LETTER

doi:10.1038/nature25477

Structural basis for DNMT3A–mediated *de novo* DNA methylation

Zhi-Min Zhang[1]†*, Rui Lu[2,3]*, Pengcheng Wang[4], Yang Yu[4], Dongliang Chen[2,3], Linfeng Gao[4], Shuo Liu[4], Debin Ji[5], Scott B Rothbart[3,6], Yinsheng Wang[4,5], Gang Greg Wang[2,3]§ & Jikui Song[1,4]§

DNA methylation by *de novo* DNA methyltransferases 3A (DNMT3A) and 3B (DNMT3B) at cytosines is essential for genome regulation and development[1,2]. Dysregulation of this process is implicated in various diseases, notably cancer. However, the mechanisms underlying DNMT3 substrate recognition and enzymatic specificity remain elusive. Here we report a 2.65-ångström crystal structure of the DNMT3A–DNMT3L–DNA complex in which two DNMT3A monomers simultaneously attack two cytosine–phosphate–guanine (CpG) dinucleotides, with the target sites separated by 14 base pairs within the same DNA duplex. The DNMT3A–DNA interaction involves a target recognition domain, a catalytic loop, and DNMT3A homodimeric interface. Arg836 of the target recognition domain makes crucial contacts with CpG, ensuring DNMT3A enzymatic preference towards CpG sites in cells. Haematological cancer-associated somatic mutations of the substrate-binding residues decrease DNMT3A activity, induce CpG hypomethylation, and promote transformation of haematopoietic cells. Together, our study reveals the mechanistic basis for DNMT3A-mediated DNA methylation and establishes its aetiological link to human disease.

Mammalian DNA methylation is an important epigenetic mechanism crucial for gene silencing and imprinting, X-inactivation, genome stability, and cell fate determination[3]. It is established mainly at CpG dinucleotides by the *de novo* methyltransferases DNMT3A and DNMT3B[1,2], and subsequently maintained by DNA methyltransferase 1 (DNMT1) in a replication-dependent manner[4]. The enzymatic function of DNMT3A and DNMT3B is further regulated by DNMT3-like protein (DNMT3L) in germ and embryonic stem (ES) cells[5–7]. Deregulation of DNMT3A and DNMT3B is associated with various human diseases including haematological cancer[8–10]. However, the molecular mechanisms underpinning DNMT3A-mediated methylation, especially substrate recognition and catalytic preference towards CpG, remain elusive. Here we generated a productive DNMT3A–DNMT3L–DNA complex using the C-terminal domains of DNMT3A and DNMT3L (Fig. 1a). The DNA molecule consists of a 10-mer central CpG-containing DNA strand annealed to an 11-mer 2′-deoxyzebularine (dZ)-containing strand (target strand), which results in a (CpG)–(dZpG) sequence context and allows formation of stable covalent DNMT3A–DNA complexes (Extended Data Fig. 1a, b). The crystal structure of the DNMT3A–DNMT3L in complex with 10/11-mer DNA, bound to cofactor by-product *S*-adenosyl-L-homocysteine (AdoHcy), was subsequently determined at 3.1 Å resolution (Extended Data Fig. 1c).

The structure of this DNMT3A–DNMT3L–DNA complex reveals a tetrameric fold arranged in the order of DNMT3L–DNMT3A–DNMT3A–DNMT3L, reminiscent of its DNA-free form[11,12] (Extended Data Figs 1d and 2a). Notably, two DNA duplexes, each bound to one DNMT3A monomer, are separated by approximately 15 Å, implying a total of 14-base-pair spacing between the two active sites of DNMT3A (Extended Data Fig. 1d). This finding prompted us to design a longer

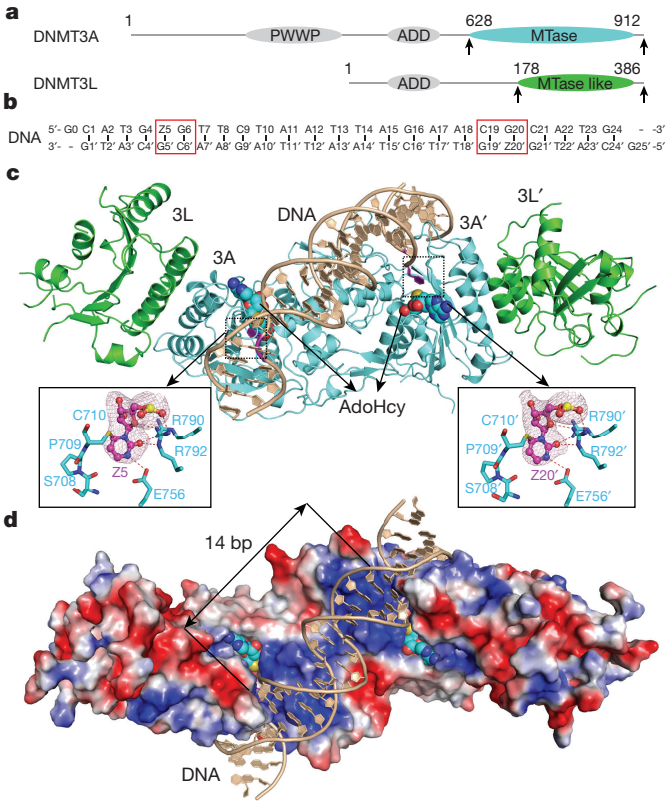

Figure 1 | Structure of the DNMT3A–DNMT3L tetramer in complex with a 25-mer DNA duplex containing two CpG sites. a, Domain architectures of DNMT3A and DNMT3L, with the C-terminal domains marked with arrowheads. **b**, DNA sequence used for structural study. Z, zebularine. **c**, **d**, Ribbon (**c**) and surface (**d**) representations of DNMT3A–DNMT3L bound to DNA and AdoHcy. The zebularines anchored at the two active sites are 14 base pairs (bp) away and shown in expanded views, with hydrogen-bonding interactions depicted as dashed lines and the $F_o - F_c$ omit map (pink) of Z5 or Z20′ contoured at the 3σ level.

[1]Department of Biochemistry, University of California, Riverside, California 92521, USA. [2]The Lineberger Comprehensive Cancer Center, University of North Carolina at Chapel Hill School of Medicine, Chapel Hill, North Carolina 27599, USA. [3]Department of Biochemistry and Biophysics, University of North Carolina at Chapel Hill School of Medicine, Chapel Hill, North Carolina 27599, USA. [4]Environmental Toxicology Graduate Program, University of California, Riverside, California 92521, USA. [5]Department of Chemistry, University of California, Riverside, California 92521, USA. [6]Center for Epigenetics, Van Andel Research Institute, Grand Rapids, Michigan 49503, USA. †Present address: School of Pharmacy, Jinan University, 601 Huangpu Avenue West, Guangzhou 510632, China.

*These authors contributed equally to this work.

§These authors jointly supervised this work.

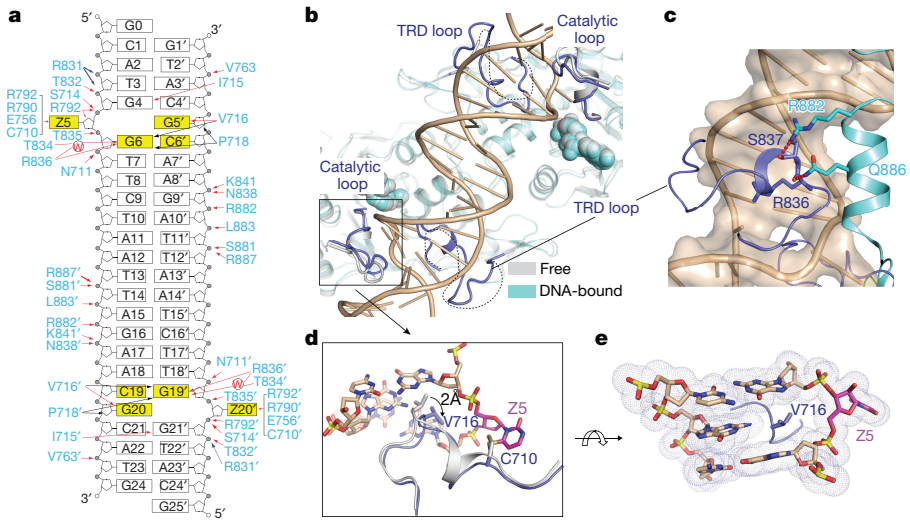

Figure 2 | Structure comparison of free and DNA-bound DNMT3A–DNMT3L tetramer. a, Schematic view of the intermolecular interactions between DNMT3A and DNA. The hydrogen-bonding, electrostatic, and van der Waals contacts are represented by red, blue, and black arrows, respectively. Water-mediated hydrogen bonds are labelled with the letter 'W'. **b**, Structural overlay of free (grey) and DNA-bound (cyan) DNMT3A–DNMT3L. The disordered TRD loops in free DNMT3A–DNMT3L are depicted as dotted lines. **c**, The TRD loop (blue) in DNA-bound DNMT3A is stabilized by hydrogen-bonding interactions (dashed lines) with R882 and Q886. **d**, Structural overlay of the catalytic loop between free (grey) and DNA-bound (blue) DNMT3A. **e**, DNA intercalation by DNMT3A V716.

DNA substrate involving a self-complementary 25-mer zebularine (Z)-containing DNA, with two (CpG)–(ZpG) sites across 14 base pairs (Fig. 1b). The structure of the DNMT3A–DNMT3L in complex with 25-mer DNA was determined at 2.65 Å resolution (Extended Data Fig. 1c), revealing only one DNA duplex bending towards the DNMT3A–DNMT3L tetramer, with the two CpG sites simultaneously anchored by two DNMT3A monomers (Fig. 1c, d and Extended Data Fig. 2b). Our data thus support the notion that the two DNMT3A monomers can co-methylate two adjacent CpG dinucleotides in one DNA-binding event[12,13]. Despite being crystallized under different conditions, both DNMT3A–DNMT3L–DNA complexes are well aligned with their DNA-free state, with a root-mean-square deviation of 0.87 Å and 1.12 Å over 790 and 826 Cα atoms, respectively (Extended Data Fig. 2a). Notably, in DNMT3A–DNMT3L–DNA complexes, zebularines are flipped out of the DNA helix and inserted deep into DNMT3A catalytic pockets, where they are covalently anchored by the catalytic cysteine C710 and hydrogen bonded to E756, R790, and R792 (Fig. 1c and Extended Data Fig. 1d). Because both structures reveal productive reaction states with consistent protein–DNA interactions, we focus on the structure of DNMT3A–DNMT3L in complex with 25-mer DNA for further analysis.

DNMT3A binding to DNA is mainly mediated by a loop from the target recognition domain (TRD) (residues R831–F848), the catalytic loop (residues G707–K721), and the homodimeric interface of DNMT3A, which together create a continuous DNA-binding surface (Figs 1d and 2a). Accordingly, these segments exhibit the most prominent structural changes upon DNA binding: the TRD loop lacked electron density in the DNA-free structure of DNMT3A–DNMT3L[11,12], but became well defined upon DNA binding and penetrated into the DNA major groove for intermolecular contacts (Fig. 2a–c); additionally, the TRD loop is stabilized through hydrogen-bonding interactions with R882, the DNMT3A mutational hotspot among leukaemias[9,10], and Q886 from an adjacent helix (Fig. 2c). Meanwhile, the catalytic loop residue V716 moves towards the DNA minor groove by approximately 2 Å, intercalating into the DNA cavity vacated because of zebularine base flipping (Fig. 2d, e). Although no protein–DNA contact was observed for DNMT3L, two DNMT3L-contacting helices of DNMT3A are preceded by DNA-binding loops (Extended Data Fig. 2c), reinforcing the notion that DNMT3L enhances DNMT3A functionality through stabilizing its DNA-binding sites[12].

Recognition of CpG dinucleotides by DNMT3A is mediated by both catalytic and TRD loops. In particular, guanine of the target strand, G6 (G19′), is specified by a hydrogen bond between its O6 atom and the Nε atom of R836 from the TRD loop, as well as water-mediated hydrogen bonds between its N7 atom and the Nε and Oγ atoms of R836 and T834, respectively (Fig. 3a). Meanwhile, the catalytic loop approaches the minor groove, where the backbone carbonyl oxygen of V716 forms a hydrogen bond with the N2 atom of the unpaired guanine G5′ (G20) (Fig. 3b). Penetration of the catalytic loop also allows V716 and P718 to engage van de Waals contacts with the base of G6 (G19′), providing additional base-specific recognition (Fig. 3b). No protein interaction was associated with C6′ (C19) of the non-target strand, providing an explanation for the observation that DNMT3A does not discriminate hemimethylated against unmethylated DNA[2]. Formation of the DNMT3A–DNA complex is also supported by various protein–DNA interactions flanking CpG, which involve electrostatic and/or hydrogen-bonding interactions of the TRD residues (R831, T832, T835, N838, and K841), catalytic loop residues (N711, S714, and I715) and DNMT3A–DNMT3A homodimeric interface residues (S881, R882, L883, and R887) with various DNA backbone or base sites (Fig. 2a and Extended Data Fig. 3a–f). These DNA-binding residues are highly conserved in DNMT3B (Extended Data Fig. 3g), suggesting a similar substrate engagement mechanism used by the DNMT3 family.

To determine the roles for CpG-engaging residues R836 and V716 in the regulation of DNMT3A activity, we performed mutagenesis followed by enzymatic studies using CpG-, CpA-, or CpT-containing substrates (Fig. 3c and Extended Data Fig. 4a, b). First, wild-type DNMT3A ($DNMT3A^{WT}$) showed methylation efficiency for CpG-containing DNA more than 20-fold higher than for CpA- or CpT-containing DNA, confirming its well-known CpG specificity[14]. By contrast, mutation of R836 to alanine (R836A) enhanced methylation of CpA- and CpT-containing DNA by 5.2- and 4.2-fold, respectively, but, as previously reported[15], only led to slight change in CpG methylation. As a result, the relative CpG/CpA and CpG/CpT preference of the $DNMT3A^{R836A}$ enzyme was reduced by 4.5- and 3.7-fold, respectively, supporting a role for R836 in substrate specificity determination. Consistent with these observations, we solved the structure of the $DNMT3A^{R836A}$–DNMT3L–DNA complex, which lacks R836-mediated hydrogen bonds to CpG without causing overall structural alterations (Extended Data Fig. 4c). Mutation of V716 to glycine (V716G) abolished methylation

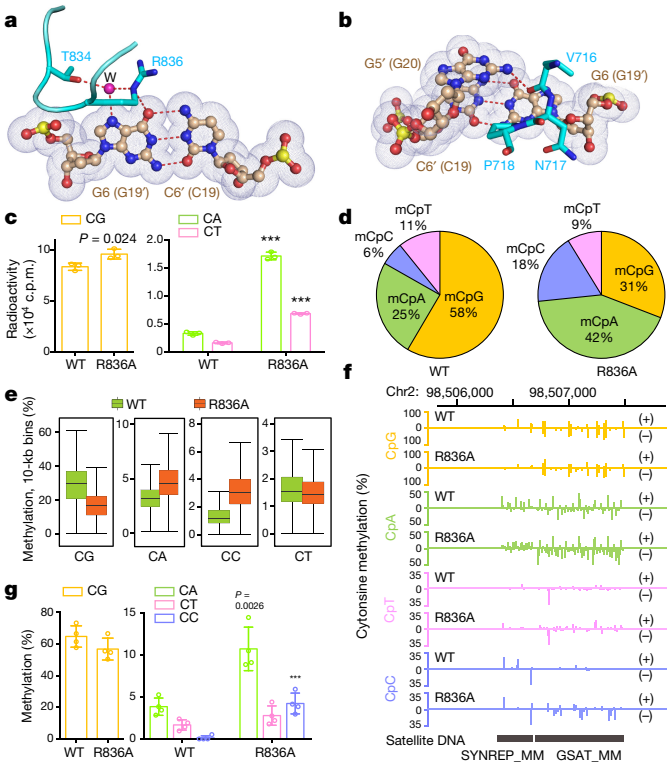

Figure 3 | DNMT3A–CpG interactions. a, **b**, Interactions of R836 (**a**) and V716-P718 (**b**) with one CpG site. The hydrogen bonds and water molecule are shown as dashed lines and a purple sphere, respectively. Nucleotides in the second CpG site are shown in parentheses. **c**, *In vitro* methylation for 40 min using DNMT3A^{WT}–DNMT3L or DNMT3A^{R836A}–DNMT3L complex ($n = 3$ biological replicates); c.p.m., counts per minute. WT, wild type. **d**, Composition of all called methylated cytosines (mC) in TKO ES cells reconstituted with DNMT3A^{WT} or DNMT3A^{R836A}. A methylated cytosine is defined using a binomial distribution-based filter with FDR less than 1% ($n = 21,678,839$ for wild type and $n = 25,272,362$ for R836A). **e**, **f**, eRRBS revealing averaged CpG and non-CpG methylations, either at global levels (**e**) or at a representative major satellite DNA region (**f**), that are induced by DNMT3A^{WT} versus DNMT3A^{R836A} among three independent lines of TKO ES cells. Shown in **e** are box and whisker plots of 10-kb-bin-averaged methylation levels for each sequence context. Symbols +/−, forward/reverse strand. The box and whiskers depict the interquartile and 1.5 × interquartile ranges, respectively. **g**, Individual bisulfite sequencing detecting the methylation level of CG, CA, CT, or CC sites within a major satellite DNA site at chromosome 2 in TKO cells expressing DNMT3A^{WT} or DNMT3A^{R836A} ($n = 4$). Data are mean ± s.d. Statistical analysis used two-tailed Student's *t*-test. ***$P < 0.001$.

of all tested substrates (Extended Data Fig. 4d). These observations support the idea that R836-mediated CpG engagement contributes to substrate specificity whereas V716-mediated intercalation is essential for DNMT3A-mediated catalysis. The increased *in vitro* activity of DNMT3A^{R836A} on CpA and CpT suggests that R836 might energetically influence the enzymology of DNMT3A, in addition to target recognition. In the case of CpG DNA, such an influence might be partly compensated by the R836-mediated hydrogen bonds, thereby ensuring the CpG specificity of DNMT3A.

Next, we introduced comparable levels of DNMT3A, either wild type or the above CpG-engagement-defective mutants, into ES cells with compound knockouts of DNMT1, DNMT3A, and DNMT3B (TKO)[16], and detected a global increase in cytosine methylation after rescue with DNMT3A^{WT} or DNMT3A^{R836A}, but not DNMT3A^{V716G} (Extended Data Fig. 4e, f). Furthermore, genome-wide methylation profiling with enhanced reduced representation bisulfite sequencing (eRRBS), followed by calling of methylation using the previously described binomial model and false discovery rate (FDR)-based threshold[17,18], revealed that, in TKO ES cells reconstituted with DNMT3A^{WT}, 58% and 42% of methylated cytosines were presented at CpG and non-CpG sites, respectively (Fig. 3d and Extended Data Fig. 5a–c); by contrast, such a distribution was reversed in cells expressing DNMT3A^{R836A}, with 31% and 69% of methylated cytosines found in CpG and non-CpG contexts (Fig. 3d and Extended Data Fig. 5b, c). Consistently, relative to wild-type controls, the absolute methylation levels were found to be decreased at CpG, but increased at CpA and CpC, sites among cells with DNMT3A^{R836A}, especially at sites showing intermediate-to-high levels of methylation (Fig. 3e and Extended Data Figs 5d and 6a). These changes were persistent among all chromosomes, at both DNA strands and over all annotated genes (Extended Data Fig. 6b–d), as exemplified by those detected at the major satellite DNA repeats (Fig. 3f) and gene-coding regions of *Foxp1* and *Dock1* (Extended Data Fig. 6e). Sanger bisulfite sequencing further validated eRRBS results at major satellite repeats in ES cells[19] (Fig. 3g and Extended Data Fig. 7). DNMT3A^{V716G} abolished both CpG and non-CpG methylations at major satellite DNA (Extended Data Fig. 7b–d). The above observation that DNMT3A^{R836A} decreases overall CpG methylations in TKO cells might be due to competition of non-CpG as a potential substrate for this mutant enzyme. Collectively, we demonstrate that engaging CpG by the R836 side chain ensures DNMT3A substrate specificity in cells.

Notably, heterozygous mutation of DNMT3A at its DNA-binding residues, such as S714, V716, P718, R792, T835, R836, N838, K841, and R882 (Figs 2a and 4a, b), occurs recurrently in haematological cancer[9,10,20] and overgrowth syndrome[21]. Although recent studies support a dominant-negative effect of the hotspot R882H mutation on DNMT3A-mediated methylation, possibly through affecting DNMT3A tetramerization[22–25], our structural observation raises the possibility that interfering with the DNA binding via residue substitution also results in functional impairment of DNMT3A during pathogenesis. Indeed, *in vitro* enzymatic assays showed the significantly reduced activity for all tested DNA-binding mutants, with the most pronounced effect observed for V716D, R792H, and K841E (Fig. 4c and Extended Data Fig. 8a–d). Consistently, expression of these three mutants in TKO ES cells failed to restore global DNA methylation (Extended Data Fig. 8e, f). It is worth noting that, although DNMT3A^{R836W} exhibited modestly reduced overall activities (Extended Data Fig. 8c, f), its activities for non-CpG methylations were found to be significantly increased at the major satellite DNA in TKO cells and in *in vitro* enzymatic assays (Extended Data Fig. 8g, h), suggesting a potential role for R836W in the redistribution of CpG versus non-CpG methylations in diseased cells. Given a largely heterozygous feature of DNMT3A mutations in leukaemia, we also queried whether the DNA-binding-defective mutants of DNMT3A inhibit functionality of DNMT3A^{WT}. To test this, we turned to a co-expression system used previously for studying the dominant-negative DNMT3A^{R882H} mutant[23], and reconstituted wild-type and mutant DNMT3A in equal amounts into TKO ES cells (Fig. 4d). Relative to expression of wild type alone, co-expression of DNMT3A^{V716D}, DNMT3A^{R792H}, or DNMT3A^{K841E} with DNMT3A^{WT} significantly decreased overall cytosine methylation (Fig. 4d). Together, we show that the DNMT3A mutants defective in substrate binding not only decrease activity but also interfere with that of DNMT3A^{WT}.

We further ectopically expressed the above DNMT3A mutants in TF-1 cells, a model used for studying leukaemia-associated gene mutation[26]. Through DNA methylation array profiling and bisulfite sequencing validation, we observed a significant reduction in overall CpG methylations in TF-1 cells stably expressing DNMT3A^{V716D}, DNMT3A^{R792H} or DNMT3A^{K841E}, relative to control; by contrast, ectopic expression of DNMT3A^{WT} induced hypermethylation (Fig. 4e and Extended Data Fig. 9). There was significant overlap among CpG sites showing hypomethylation due to expression of DNMT3A^{V716D}, DNMT3A^{R792H}, or DNMT3A^{K841E} (Extended Data Fig. 10a), indicating their common effect on epigenomic deregulation. Reduced methylation

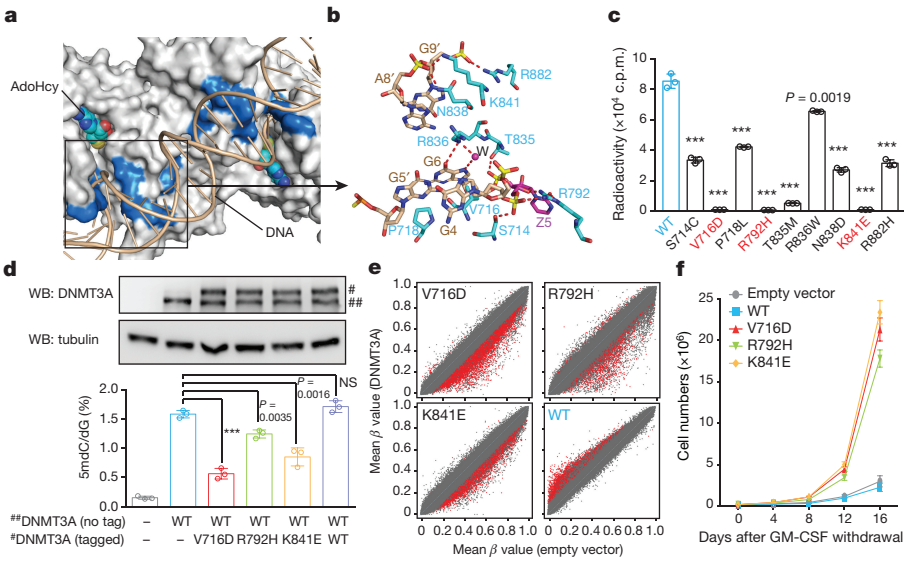

Figure 4 | Haematological cancer-associated mutations of the DNMT3A–DNA interaction residues. a, **b**, Surface (**a**) and stick (**b**) views of the DNA-contacting residues in DNMT3A found mutated in haematological cancer. Mutation sites are coloured blue in **a**. The hydrogen-bonding interactions and water molecule are shown as dashed lines and a purple sphere, respectively. **c**, *In vitro* methylation of CpG DNA using DNMT3A^{WT} or its haematological cancer-associated mutants ($n = 3$). **d**, DNMT3A immunoblots (top) and liquid chromatography–tandem mass spectrometry (LC–MS/MS and MS/MS/MS)-based quantification of 5-methyl-2′-deoxycytidine (5-mdC; bottom, $n = 3$ biological replicates) in DNA isolated from TKO ES cells re-expressing DNMT3A^{WT} alone (##, non-tagged) or together with the equal amount of the indicated DNMT3A mutant (#, tagged). A representative blot of two independent experiments is shown. For gel Source Data, see Supplementary Fig. 1. **e**, Scatter plots showing mean methylation β values of each individual CpG among TF-1 cells with stable expression of the indicated DNMT3A mutant (y axis; $n = 3$–8 biological replicates) compared with empty vector controls (x axis), with significantly differentially methylated CpGs depicted in red. **f**, Proliferation of the indicated DNMT3A-expressing TF-1 cells under cytokine-poor conditions ($n = 3$). Data are mean ± s.d. Statistical analysis used two-tailed Student's t-test. ***$P < 0.001$.

of these commonly affected sites was also detected after transduction of other leukaemia-associated substrate-binding mutations of DNMT3A (P718L, T835M, R836W, and N838D), although it did not induce hypomethylation globally (Extended Data Fig. 10b, c). Binding of wild-type or mutant DNMT3A was comparable at tested loci showing methylation changes (Extended Data Fig. 10d, e). Given that epigenetic deregulation promotes TF-1 cell transformation characterized by cytokine-independent growth[26], we queried whether the DNA-binding-defective mutation of DNMT3A causes a similar transformation of this model. We found that, under cytokine-supporting conditions, TF-1 cells expressing wild-type or mutant DNMT3A exhibited comparable proliferation (Extended Data Fig. 10f). By contrast, those expressing a DNA-binding-defective mutant, but not DNMT3A^{WT}, had significant cytokine-independent growth capability (Fig. 4f and Extended Data Fig. 10g). Collectively, we demonstrate that the DNA-binding residues of DNMT3A are vital for establishing appropriate CpG methylation in haematological cells and that their somatic mutations detected in patients with leukaemia promote transformation.

Online Content Methods, along with any additional Extended Data display items and Source Data, are available in the online version of the paper; references unique to these sections appear only in the online paper.

Received 17 January; accepted 21 December 2017.
Published online 7 February 2018.

1. Okano, M., Bell, D. W., Haber, D. A. & Li, E. DNA methyltransferases Dnmt3a and Dnmt3b are essential for *de novo* methylation and mammalian development. *Cell* **99,** 247–257 (1999).
2. Okano, M., Xie, S. & Li, E. Cloning and characterization of a family of novel mammalian DNA (cytosine-5) methyltransferases. *Nat. Genet.* **19,** 219–220 (1998).
3. Bird, A. DNA methylation patterns and epigenetic memory. *Genes Dev.* **16,** 6–21 (2002).
4. Goll, M. G. & Bestor, T. H. Eukaryotic cytosine methyltransferases. *Annu. Rev. Biochem.* **74,** 481–514 (2005).
5. Bourc'his, D., Xu, G. L., Lin, C. S., Bollman, B. & Bestor, T. H. Dnmt3L and the establishment of maternal genomic imprints. *Science* **294,** 2536–2539 (2001).
6. Chedin, F., Lieber, M. R. & Hsieh, C. L. The DNA methyltransferase-like protein DNMT3L stimulates *de novo* methylation by Dnmt3a. *Proc. Natl Acad. Sci. USA* **99,** 16916–16921 (2002).
7. Hata, K., Okano, M., Lei, H. & Li, E. Dnmt3L cooperates with the Dnmt3 family of *de novo* DNA methyltransferases to establish maternal imprints in mice. *Development* **129,** 1983–1993 (2002).
8. Robertson, K. D. DNA methylation and human disease. *Nat. Rev. Genet.* **6,** 597–610 (2005).
9. Yang, L., Rau, R. & Goodell, M. A. DNMT3A in haematological malignancies. *Nat. Rev. Cancer* **15,** 152–165 (2015).
10. Ley, T. J. *et al.* DNMT3A mutations in acute myeloid leukemia. *N. Engl. J. Med.* **363,** 2424–2433 (2010).
11. Guo, X. *et al.* Structural insight into autoinhibition and histone H3-induced activation of DNMT3A. *Nature* **517,** 640–644 (2015).
12. Jia, D., Jurkowska, R. Z., Zhang, X., Jeltsch, A. & Cheng, X. Structure of Dnmt3a bound to Dnmt3L suggests a model for *de novo* DNA methylation. *Nature* **449,** 248–251 (2007).
13. Jurkowska, R. Z. *et al.* Formation of nucleoprotein filaments by mammalian DNA methyltransferase Dnmt3a in complex with regulator Dnmt3L. *Nucleic Acids Res.* **36,** 6656–6663 (2008).
14. Gowher, H. & Jeltsch, A. Enzymatic properties of recombinant Dnmt3a DNA methyltransferase from mouse: the enzyme modifies DNA in a non-processive manner and also methylates non-CpA sites. *J. Mol. Biol.* **309,** 1201–1208 (2001).
15. Gowher, H. *et al.* Mutational analysis of the catalytic domain of the murine Dnmt3a DNA-(cytosine C5)-methyltransferase. *J. Mol. Biol.* **357,** 928–941 (2006).
16. Tsumura, A. *et al.* Maintenance of self-renewal ability of mouse embryonic stem cells in the absence of DNA methyltransferases Dnmt1, Dnmt3a and Dnmt3b. *Genes Cells* **11,** 805–814 (2006).
17. Guo, J. U. *et al.* Distribution, recognition and regulation of non-CpG methylation in the adult mammalian brain. *Nat. Neurosci.* **17,** 215–222 (2014).
18. Lister, R. *et al.* Human DNA methylomes at base resolution show widespread epigenomic differences. *Nature* **462,** 315–322 (2009).
19. Chen, T., Tsujimoto, N. & Li, E. The PWWP domain of Dnmt3a and Dnmt3b is required for directing DNA methylation to the major satellite repeats at pericentric heterochromatin. *Mol. Cell. Biol.* **24,** 9048–9058 (2004).
20. Forbes, S. A. *et al.* COSMIC: exploring the world's knowledge of somatic mutations in human cancer. *Nucleic Acids Res.* **43,** D805–D811 (2015).
21. Tatton-Brown, K. *et al.* Mutations in the DNA methyltransferase gene DNMT3A cause an overgrowth syndrome with intellectual disability. *Nat. Genet.* **46,** 385–388 (2014).
22. Holz-Schietinger, C., Matje, D. M. & Reich, N. O. Mutations in DNA methyltransferase (DNMT3A) observed in acute myeloid leukemia patients disrupt processive methylation. *J. Biol. Chem.* **287,** 30941–30951 (2012).

23. Kim, S. J. *et al.* A DNMT3A mutation common in AML exhibits dominant-negative effects in murine ES cells. *Blood* **122,** 4086–4089 (2013).
24. Lu, R. *et al.* Epigenetic perturbations by Arg882-mutated DNMT3A potentiate aberrant stem cell gene-expression program and acute leukemia development. *Cancer Cell* **30,** 92–107 (2016).
25. Russler-Germain, D. A. *et al.* The R882H DNMT3A mutation associated with AML dominantly inhibits wild-type DNMT3A by blocking its ability to form active tetramers. *Cancer Cell* **25,** 442–454 (2014).
26. Losman, J. A. *et al.* (*R*)-2-hydroxyglutarate is sufficient to promote leukemogenesis and its effects are reversible. *Science* **339,** 1621–1625 (2013).

Supplementary Information is available in the online version of the paper.

Acknowledgements We thank X. Cheng for comments on the manuscript, M. Okano, J. Wang, and J.-A. Losman for providing reagents used in the study, and staff members at the Advanced Light Source, Lawrence Berkeley National Laboratory, and at the Advanced Photo Source, Argonne National Laboratory, for access to X-ray beamlines. We are also grateful for the support of University of North Carolina facilities including Genomics Core, which are partly supported by UNC Cancer Center Core Support Grant P30-CA016086. This work was supported by Kimmel Scholar Awards (to J.S. and G.G.W.), the March of Dimes Foundation (1-FY15-345 to J.S.), the DoD Peer-reviewed Cancer Research Program (W81XWH-14-1-0232 to G.G.W.), Gabrielle's Angel Foundation for Cancer Research (to G.G.W.), Gilead Sciences Research Scholars Program in haematology/oncology (to G.G.W.), University Cancer Research Fund of the N.C. state (to G.G.W.), and the National Institutes of Health (1R35GM119721 to J.S.; R35GM124736 to S.B.R.; 5R21ES025392 to Y.W.; and 1R01CA215284, 1R01CA218600, and 1R01CA211336 to G.G.W.). G.G.W. is a Research Scholar of American Cancer Society and a Junior Faculty Scholar of American Society of Haematology. R.L. was supported by a Lymphoma Research Foundation postdoctoral fellowship.

Author Contributions Z.-M.Z., R.L., P.W., Y.Y., D.C., L.G., S.L., D.J., and J.S. performed experiments. S.B.R. provided technical support. Y.W., G.G.W., and J.S. conceived and organized the study. Z.-M.Z., R.L., G.G.W., and J.S. prepared the manuscript.

Author Information Reprints and permissions information is available at www.nature.com/reprints. The authors declare no competing financial interests. Readers are welcome to comment on the online version of the paper. Publisher's note: Springer Nature remains neutral with regard to jurisdictional claims in published maps and institutional affiliations. Correspondence and requests for materials should be addressed to J.S. (jikui.song@ucr.edu) or G.G.W. (greg_wang@med.unc.edu).

Reviewer Information *Nature* thanks A. Jeltsch, R. Xu and the other anonymous reviewer(s) for their contribution to the peer review of this work.

METHODS

Protein expression and purification. The gene fragments encoding residues 628–912 of human DNMT3A (NCBI accession number NM_022552) and residues 178–386 of human DNMT3L were inserted in tandem into a modified pRSFDuet-1 vector (Novagen). The DNMT3A sequence was separated from the preceding His_6-SUMO tag by a ubiquitin-like protease (ULP1) cleavage site. Expression and purification of the DNMT3A–DNMT3L complex followed a previously described protocol[27]. In brief, the His_6-SUMO–DNMT3A fusion protein and DNMT3L were co-expressed in *Escherichia coli* BL21 DE3 (RIL) cell strains and purified using a Ni^{2+}-NTA column. Subsequently, the His_6-SUMO tag was removed through ULP1-mediated cleavage, followed by ion exchange chromatography on a Heparin column. For enzymatic assays, the DNMT3A–DNMT3L complex was further purified through size-exclusion chromatography on a HiLoad 16/600 Superdex 200 pg column (GE Healthcare), and concentrated to 0.1–0.3 mM in a buffer containing 20 mM Tris-HCl (pH 8.0), 100 mM NaCl, 0.1% β-mercaptoethanol, and 5% glycerol. To generate the covalent DNMT3A–DNMT3L–DNA complex, an 11-mer single-stranded DNA that was in-house synthesized to contain 2′-deoxy zebularine[28] (5′-CATGdZGCTCTC-3′; dZ, 2′-deoxyzebularine) was annealed with a 10-mer single-stranded DNA (5′-AGAGCGCATG-3′) before reaction with the DNMT3A–DNMT3L complex in the presence of 20 mM Tris-HCl (pH 7.5), 50 mM NaCl, 20% glycerol, and 40 mM DTT at room temperature. In addition, a 25-mer zebularine-containing DNA (5′-GCATGZGTTCTAATTAGAACGCATG-3′; Z, zebularine) was self-annealed and used to form a second DNMT3A–DNMT3L–DNA complex or the $DNMT3A^{R836A}$–DNMT3L–DNA complex. The reaction products were further purified through a HiTrap Q XL column (GE Healthcare), followed by size-exclusion chromatography on a HiLoad 16/600 Superdex 200 pg column. The final samples for crystallization of the productive DNMT3A–DNMT3L–DNA complexes contained about 0.1–0.2 mM covalent DNMT3A–DNMT3L–DNA complexes, 0.3 mM AdoHcy, 20 mM Tris-HCl (pH 8.0), 100 mM NaCl, 0.1% β-mercaptoethanol, and 5% glycerol.

Crystallization conditions and structure determination. The crystals for the covalent complex of DNMT3A–DNMT3L with the 10/11-mer DNA were generated by the hanging-drop vapour-diffusion method at 23 °C, from drops mixed from 0.5 μl of DNMT3A–DNMT3L–DNA solution and 0.5 μl of precipitant solution (7% PEG4000, 0.1 M Tris-HCl (pH 8.5), 100 mM $MgCl_2$, 166 mM imidazole (pH 7.0)). The reproducibility and quality of crystals were further improved by the micro-seeding method. The crystals were soaked in cryoprotectant made of mother liquor supplemented with 30% PEG400, before being flash frozen in liquid nitrogen. For the complex of DNMT3A (either wild-type or R836A mutant) with DNMT3L and the 25-mer DNA, crystals were generated by the hanging-drop vapour-diffusion method at 4 °C, from drops mixed from 1.5 μl of the protein solution and 1.5 μl of precipitation solution (0.1 M Tris-HCl (pH 7.0), 200 mM NaH_2PO_4, and 5% PEG4000). The crystals were treated with cryoprotectant containing the precipitation solution and 30% glycerol before collecting.

X-ray diffraction datasets for the covalent DNMT3A–DNMT3L–DNA complexes were collected at selenium peak wavelength on the BL501 or BL502 beamlines at the Advanced Light Source, Lawrence Berkeley National Laboratory, and the dataset for the covalent DNMT3A (R836A)–DNMT3L–DNA complex was collected on the 24-ID-E NE-CAT beamline at the Advanced Photon Source, Argonne National Laboratory. The diffraction data were indexed, integrated, and scaled using the HKL 2000 program[29] or the XDS program[30]. The structures of the productive covalent complexes of DNMT3A–DNMT3L–DNA were solved using the molecular replacement method in PHASER[31], with the DNA-free structure of DNMT3A–DNMT3L (PDB 2QRV) serving as a search model. Further modelling of the covalent DNMT3A–DNMT3L–DNA complexes was performed using COOT[32] and then subject to refinement using the PHENIX software package[33]. The same R-free test set was used throughout the refinement. The final models for DNMT3A–DNMT3L complexed with the 25-mer and 10/11-mer DNAs were refined to 2.65 Å and 3.1 Å resolution, respectively. The final model for DNMT3A (R836A)–DNMT3L complexed with the 25-mer DNA was refined to 3.0 Å resolution.

The statistics for data collection and structural refinement of the productive covalent DNMT3A–DNMT3L–DNA complexes are summarized in Extended Data Fig. 1c.

***In vitro* DNA methylation assay.** Synthesized $(GAC)_{12}$, $(AAC)_{12}$ and $(TAC)_{12}$ DNA duplexes were used as CG-, CA- and CT-containing substrates, respectively. The DNA methylation assays were performed in triplicate at 37 °C for 1 h, unless otherwise indicated. In brief, a 20-μl reaction mixture contained 2.5 μM *S*-adenosyl-L-[methyl-^{3}H]methionine (AdoMet) (specific activity 18 Ci mmol^{-1}, PerkinElmer), 0.3 μM DNMT3A–DNMT3L, 0.75 μM DNA in 59 mM Tris-HCl, pH 8.0, 0.05% β-mercaptoethanol, 5% glycerol, and 200 μg ml^{-1} BSA. The methylation reactions were stopped by flash freezing in liquid nitrogen, followed by precipitation and incubation on ice for 1 h, in 1 ml of 15% trichloroacetic acid solution plus 40 μg ml^{-1} BSA. The trichloroacetic acid-precipitated samples were then passed through a GF/C filter (GE Healthcare) using a vacuum-filtration apparatus. After sequential washing with 2 × 5 ml of cold 10% trichloroacetic acid and 5 ml of ethanol, the filters were dried and transferred to scintillation vials filled with 5 ml of ScintiVerse (Fisher), followed by measurement of tritium scintillation with a Beckman LS6500 counter.

Plasmid construction. Full-length human DNMT3A isoform 1 was cloned into the EcoRI site of the pPyCAGIZ vector (a gift from J. Wang). DNMT3A mutation was generated by a QuikChange II XL Site-Directed Mutagenesis Kit (Agilent). To achieve co-expression of the wild-type and mutant DNMT3A at equal levels in cells, we engineered a T2A-based fusion construct consisting of the mutant cDNA, which was added with an N-terminal 3× Flag–$(GGGGS)_3$-Myc tag to differentiate its protein size from non-tagged wild-type DNMT3A, followed by a T2A peptide sequence at its C terminus and the cDNA of non-tagged wild-type DNMT3A. Myc-tagged full-length human DNMT3A isoform 1 was cloned into MSCV Pac retroviral vector as previously described[24]. All plasmid sequences were verified by sequencing.

Cell lines and cell culture. *Dnmt3a*, *Dnmt3b*, and *Dnmt1* TKO mouse ES cells (a gift from M. Okano)[16] were cultivated on gelatin-coated dishes in the high-glucose DMEM base medium (Invitrogen) supplemented with 15% of fetal bovine serum (FBS, Invitrogen), 1× non-essential amino acids (Invitrogen), 0.1 mM β-mercaptoethanol, and 1,000 U ml^{-1} leukaemia inhibitory factor (ESGRO). The TF-1 human erythroleukaemic cell line was obtained from American Type Culture Collection (ATCC) and cultivated in the RPMI 1640 base medium (Invitrogen) supplemented with 10% of FBS and 2 ng ml^{-1} of recombinant human granulocyte–macrophage colony-stimulating factor (GM-CSF; R&D Systems). Acquisition of the cytokine-independent growth of TF-1 cells by the introduction of cancer-associated gene mutation was examined and quantified upon GM-CSF removal as previously described[26].

Authentication of cell line identities, including those of parental and derived lines, was ensured by the Tissue Culture Facility affiliated to the University of North Carolina at Chapel Hill Lineberger Comprehensive Cancer Center using the genetic signature profiling and fingerprinting analysis previously described[34]. Every 1–2 months, a routine examination of cell lines in culture for any possible mycoplasma contamination was performed using commercially available detection kits (Lonza Walkersville).

Generation of stable cell lines. TKO ES cells were transfected by Lipofectamine 2000 (Invitrogen) with the pPyCAGIZ empty vector or that carrying wild-type or mutant DNMT3A. Forty-eight hours after transfection, the transduced ES cells were selected out in 50 μg ml^{-1} Zeocin (Invitrogen) for 10 days. The pooled stable-expression cell lines and independent single-cell-derived clonal lines were continuously maintained in the medium with 25 μg ml^{-1} zeocin. To generate TF-1 leukaemia cell lines with stable expression of wild-type or mutant DNMT3A, the MSCV-based retrovirus was packaged in HEK293 cells and used for infection as previously described[35]. Forty-eight hours after infection, TF-1 cells were selected by 2 μg ml^{-1} puromycin for 4 days and maintained in medium with 1 μg ml^{-1} puromycin.

Western blotting. Antibodies used for western blotting were anti-MYC (Sigma-Aldrich, 9E10), anti-DNMT3A (Santa Cruz, H-295), anti-β-actin (Santa Cruz, sc-47778), and α-tubulin (Sigma-Aldrich). Total protein samples were prepared by cell lysis with SDS-containing Laemmli sample buffer followed by brief sonication. Extracted samples equivalent to 100,000 cells were loaded to the SDS–PAGE gels for western blot analysis.

Quantification of 5-methyl-2′-deoxycytidine and 2′-deoxyguanosine in genomic DNA. The measurement procedures for 5-methyl-2′-deoxycytidine (5-mdC) and 2′-deoxyguanosine in genomic DNA were described previously[36,37]. In brief, 1 μg of genomic DNA prepared from cells was enzymatically digested into nucleoside mixtures. Enzymes in the digestion mixture were removed by chloroform extraction, and the resulting aqueous layer was concentrated to 10 μl and subjected directly to LC–MS/MS and LC–MS/MS/MS analysis for quantification of 5-mdC and 2′-deoxyguanosine, respectively. The amounts of 5-mdC and 2′-deoxyguanosine (in moles) in the nucleoside mixtures were calculated from area ratios of peaks found in selected-ion chromatograms for the analytes over their corresponding isotope-labelled standards, the amounts of the labelled standards added (in moles), and the calibration curves. The final levels of 5-mdC, in terms of percentages of 2′-deoxyguanosine, were calculated by comparing the amounts of 5-mdC relative to those of 2′-deoxyguanosine.

eRRBS and data analysis. Genomic DNA of each sample was added with 0.5% of unmethylated lambda DNA (Promega) as a spike-in control and subjected to eRRBS using MethylMidi-seq (Zymo Research) as described before[24]. In brief, approximately 300 ng of DNA were digested with three restriction enzymes (80 units of MspI, 40 units of BfaI, and 40 units of MseI) to improve genomic DNA fragmentation and coverage. The generated DNA fragments were ligated

to the pre-annealed 5-methyl-cytosine-containing adapters, followed by filling in overhangs and the A extension at the 3′ terminus. The DNA fragments were then purified and subjected to bisulfite treatment using an EZ DNA Methylation–Lightning Kit (Zymo Research). After amplification, the quality of eRRBS libraries was checked with Agilent 2200 TapeStation, followed by deep sequencing using an Illumina HiSeq-2000 genome analyser (50 base pairs and paired end as parameters). Obtained reads were aligned to *in silico* bisulfite-converted mouse reference genome mm9 and lambda DNA sequence (GenBank accession number J02459.1) using the Bismark package in a strand-specific manner[38]. For identification of methylated cytosines, all mapped cytosines were subjected to a binomial distribution model-based methylation calling as described in the scetion below. To determine distribution of methylation levels, only those high-quality reads with at least 15 times coverage were used. For convenience of data analysis and to increase data complexity, data from all three biological replicates were merged and cytosine sites covered with at least 15 reads in the merged dataset were used for downstream analysis such as averaged methylation levels in 10-kb window sliding and aggregated methylation levels across genes. Data representation and plots were generated with the 'ggplot2' package in R software using custom scripts.

Identification of methylated cytosines. We used a previously described binomial model to identify methylated cytosines[17,18]. Specifically, with the unmethylated spike-in lambda DNA, we first determined the bisulfite non-conversion rate (probability, *P*) for each cytosine sequence context independently (that is, CpG, CpA, CpC, and CpT). For each mapped cytosine in our eRRBS data, we calculated the binomial *P* value in which methylated reads occurred out of the total read number on the basis of the binomial test, with the bisulfite non-conversion rate as the success probability (*P*). If a *P* value was under a threshold, we defined the cytosine as truly methylated. To determine the FDR for each different threshold, we created a control methylome for each eRRBS sample. In the control methylome, read depth at each cytosine was equal to the real data, and the methylated events were simulated by binomial distribution using the previously defined non-conversion rate (*P*). The FDR was determined by the ratio between the number of identified methylated cytosine sites from the control methylome and that from the real data. For each eRRBS sample, we chose to use a *P* value under which the FDR was less than 1% or 0.1%, as specified in figure legends.

DNA methylation array and data analysis. Genomic DNA was extracted and bisulfite-converted as described above. DNA methylation profiling using an Illumina Infinium HumanMethylation450 BeadChip array was performed by the UNC Genomics Core according to the manufacturer's instructions. Methylation data were then subject to background subtraction and control normalization by executing preprocessIllumina in the R 'minfi' package[39]. Differentially methylated CpGs were identified using dmpFinder in a categorical mode. Methylation changes were considered significant at a q-value of less than 0.05 and a β value difference of more than 0.1. Hierarchical clustering analysis, scatter plots, and density plots were generated in R using 'pheatmap' and 'ggplot2' packages.

Sanger bisulfite sequencing. Sanger bisulfite sequencing was performed as previously described[24]. In brief, genomic DNA was prepared using a DNeasy Blood and Tissue Kit (Qiagen) and 1 μg genomic DNA subject to bisulfite conversion using an EZ DNA Methylation Gold Kit according to manufacturer's instructions (Zymo Research). Bisulfite-treated DNA was then used as template in PCR to amplify the target DNA region, followed by cloning of PCR products into pCR2.1-TOPO vector (Invitrogen) for direct sequencing of individual clones. Four biological replicates per cell line were tested, with at least ten clonal sequences per replicate generated. The primers used for amplifying a major satellite DNA sequence located at chromosome 2 were 5′-GGG AAT TTT GGT GGT AGG GT-3′ and 5′-AAA AAA CAT CCA CTT AAC TAC TTA AAA A-3′. The primers used for validating 450k array data were, for EIF4G1, 5′-AGG AGA TTG AGG TTT TAG TGA ATA TGT-3′ and 5′-CCC TAT ATC AAA TTC TTC CTA CCA TAA-3′; for HDLBP, 5′-GGA GGT GAA GTT ATG GAG ATA TTT TT-3′ and 5′-ATC CCA TAC CAA CAA AAA CTA ACA A-3′; for FOXK2, 5′-TAT GTT TGT ATT TGG GGT GTT TTT T-3′ and 5′-CTA AAA AAT CAA AAA CAT TTC CTA CC-3′.

Chromatin immunoprecipitation. Samples used for chromatin immunoprecipitation (ChIP) were prepared as previously described[8]. In brief, chromatin samples extracted from cells expressing Myc-tagged DNMT3A were used for ChIP with the 9E10 anti-Myc antibody (Sigma-Aldrich), with cells expressing empty vector used as negative control. Real-time PCR was performed for detecting DNMT3A binding at sites listed below. The primers for ChIP-PCR at each tested site were as follows: for cg23189692, 5′-TTG GCA TGC TCA CAG AGA GG-3′ and 5′-GTC TTC CCA GGC TCA TTG CT-3′; for cg00704780. 5′-AGC AAA ACG GTC AGT AGC CA-3′ and 5′-TAC CAG CAA AAG CTG GCA GG-3′; for cg10460657, 5′-GCC TCT GAC CTG CTG TCT AC-3′ and 5′-AGG AAA TGC CCC AGA CGT G-3′; for cg07564962, 5′-GGC CGG CAC TAA TGT CTT TC-3′ and 5′-TTC CCT GCT CTG TGG GAA GG-3′; for cg13393476, 5′-CCT TGC GAG TGA GTC ACG G-3′ and 5′-GAG ATT CTG CCA GGC TCC AC-3′; for cg20509869, 5′-GTG GGA CGC TAA CCC TCT TC-3′ and 5′-GGC GGC TGA TTT ATC TGG GT-3′; and for GAPDH transcription start site, 5′-TCT CCC CAC ACA CAT GCA CTT-3′ and 5′-CCT AGT CCC AGG GCT TTG ATT-3′.

Statistics. No statistical methods were used to predetermine sample size. The experiments were not randomized. The investigators were not blinded to allocation during experiments and outcome assessment. Data are presented as the mean ± s.d. of at least three independent experiments. Statistical analysis was performed with a Student's *t*-test for comparing two sets of data with assumed normal distribution. A *P* value of less than 0.05 was considered to be significant.

Code availability. The scripts for genomic data analyses and all other data are available from the corresponding authors upon reasonable request.

Data availability. Coordinates and structure factors for DNMT3A–DNMT3L in complex with 25-mer DNA, DNMT3A–DNMT3L in complex with 10/11-mer DNA, and DNMT3A (R836A)–DNMT3L in complex with 25-mer DNA have been deposited in the Protein Data Bank under accession numbers 5YX2, 6F57, and 6BRR, respectively. The eRRBS and Illumina Human Methylation 450K array data have been deposited in NCBI Gene Expression Omnibus under accession number GSE99391.

27. Song, J., Rechkoblit, O., Bestor, T. H. & Patel, D. J. Structure of DNMT1-DNA complex reveals a role for autoinhibition in maintenance DNA methylation. *Science* **331,** 1036–1040 (2011).
28. Zhou, L. *et al.* Zebularine: a novel DNA methylation inhibitor that forms a covalent complex with DNA methyltransferases. *J. Mol. Biol.* **321,** 591–599 (2002).
29. Otwinowski, Z. & Minor, W. Processing of X-ray diffraction data collected in oscillation mode. *Methods Enzymol.* **276,** 307–326 (1997).
30. Kabsch, W. Xds. *Acta Crystallogr. D* **66,** 125–132 (2010).
31. McCoy, A. J. *et al.* Phaser crystallographic software. *J. Appl. Crystallogr.* **40,** 658–674 (2007).
32. Emsley, P. & Cowtan, K. Coot: model-building tools for molecular graphics. *Acta Crystallogr. D* **60,** 2126–2132 (2004).
33. Adams, P. D. *et al.* PHENIX: building new software for automated crystallographic structure determination. *Acta Crystallogr. D* **58,** 1948–1954 (2002).
34. Yu, M. *et al.* A resource for cell line authentication, annotation and quality control. *Nature* **520,** 307–311 (2015).
35. Wang, G. G. *et al.* Quantitative production of macrophages or neutrophils *ex vivo* using conditional Hoxb8. *Nat. Methods* **3,** 287–293 (2006).
36. Volz, D. C. *et al.* Tris(1,3-dichloro-2-propyl)phosphate induces genome-wide hypomethylation within early zebrafish embryos. *Environ. Sci. Technol.* **50,** 10255–10263 (2016).
37. Yu, Y. *et al.* Comprehensive assessment of oxidatively induced modifications of DNA in a rat model of human Wilson's disease. *Mol. Cell. Proteomics* **15,** 810–817 (2016).
38. Krueger, F. & Andrews, S. R. Bismark: a flexible aligner and methylation caller for Bisulfite-Seq applications. *Bioinformatics* **27,** 1571–1572 (2011).
39. Aryee, M. J. *et al.* Minfi: a flexible and comprehensive Bioconductor package for the analysis of Infinium DNA methylation microarrays. *Bioinformatics* **30,** 1363–1369 (2014).

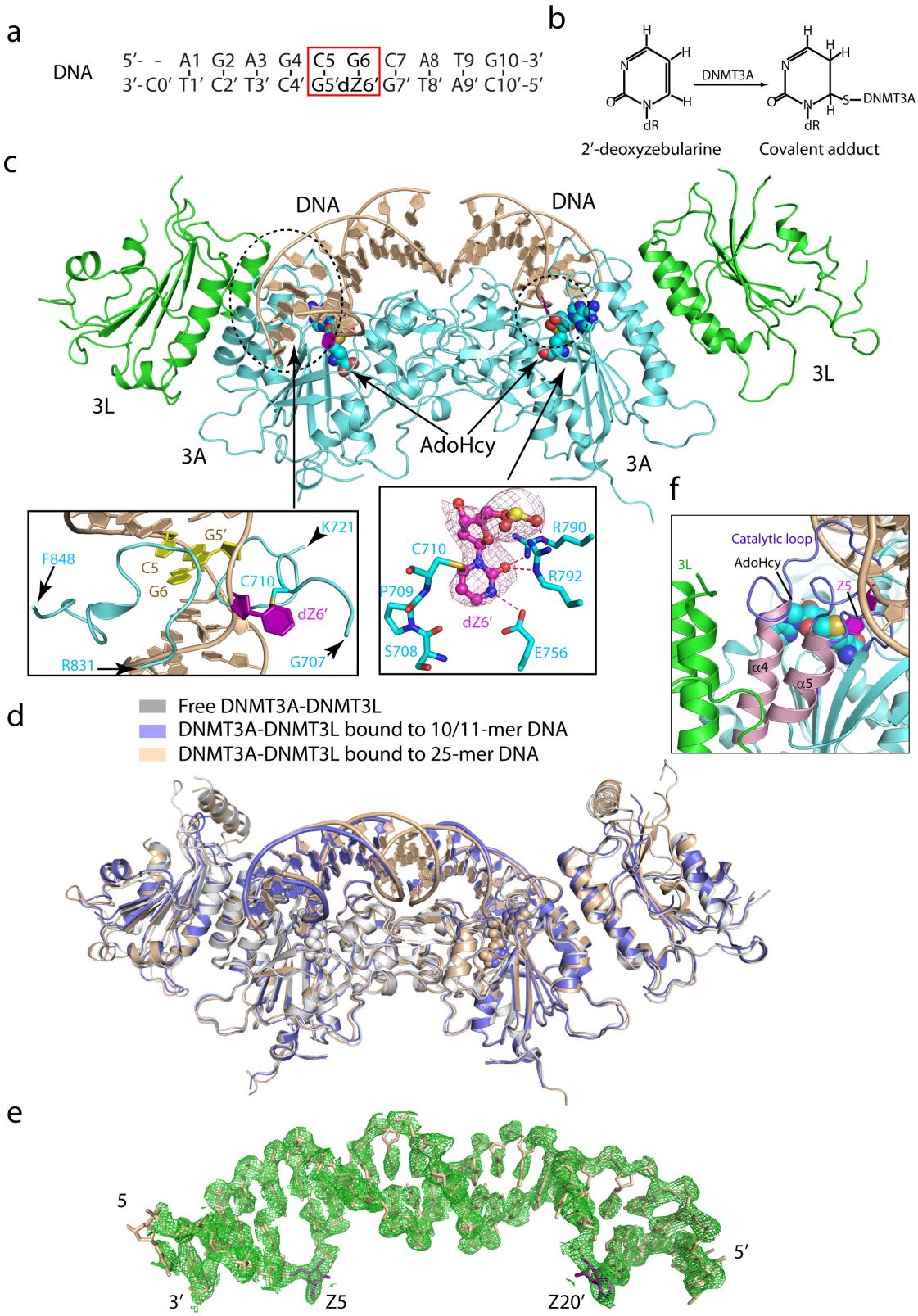

Extended Data Figure 1 | Structures of the DNMT3A–DNMT3L tetramer in complex with the 10/11-mer DNA. a, The sequence of the 10/11-mer DNA duplex used for structural study. **b**, Chemical formula of the covalent adduct of DNMT3A and 2′-deoxyzebularine. **c**, Data collection and refinement statistics. Each dataset was collected from a single crystal. **d**, Ribbon representations of the DNMT3A–DNMT3L tetramer in complex with the 10/11-mer DNA duplex and AdoHcy. DNMT3A, DNMT3L, and DNA are coloured in light blue, green, and wheat, respectively, and AdoHcy shown in sphere representation. The boxed areas show expanded views for the CpG sites (purple and yellow), the DNA-binding TRD and catalytic loops (left box), and the flipped out 2′-deoxyzebularine (dZ6′) surrounded by conserved catalytic residues (right box). The $F_o - F_c$ omit map of 2′-deoxyzebularine (pink) is contoured at the 3σ level. The hydrogen-bonding interactions are depicted as dashed lines.

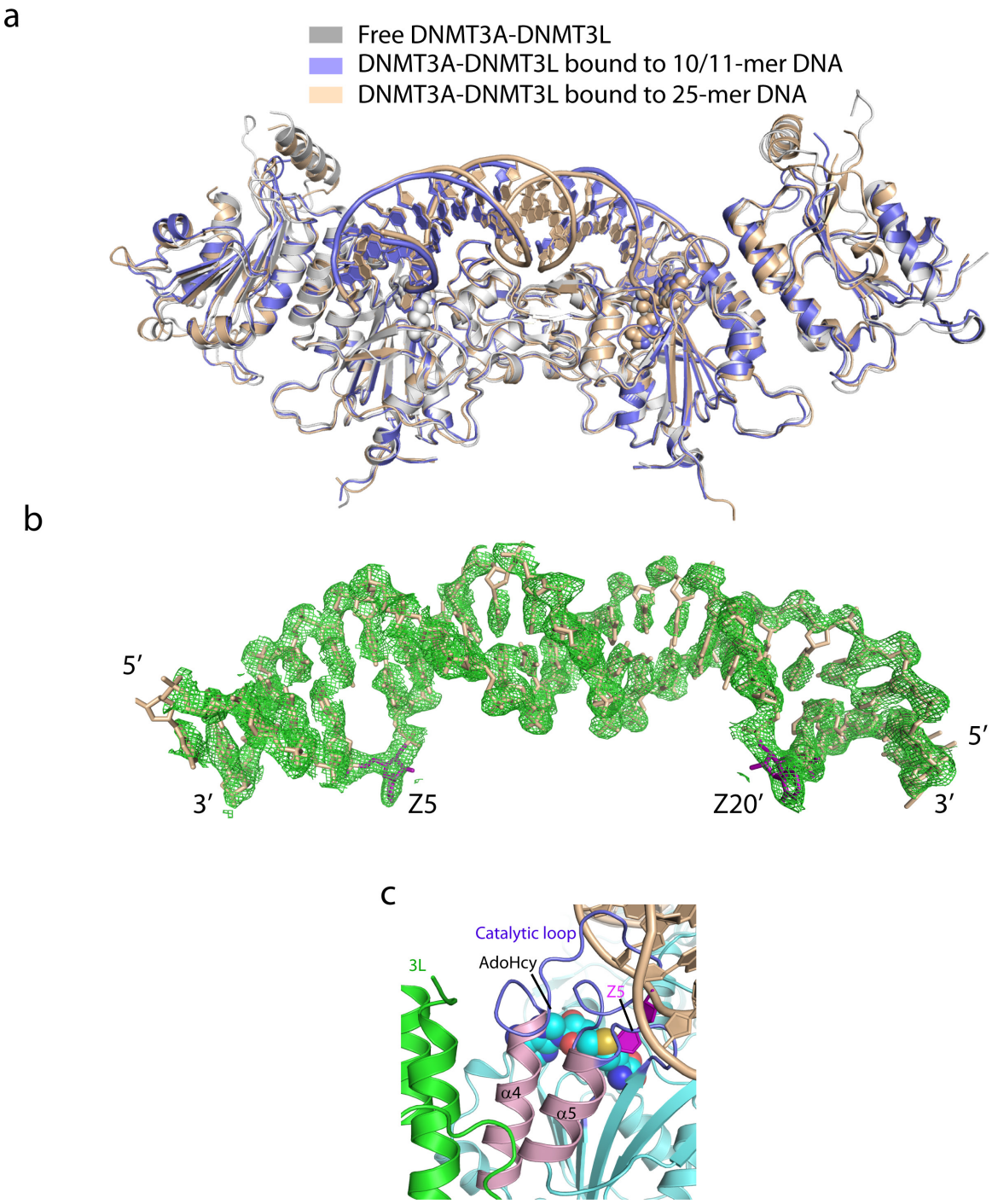

Extended Data Figure 2 | Intermolecular interactions between the DNMT3A–DNMT3L tetramer and DNA. a, Structural overlay of free DNMT3A–DNMT3L (PDB 2QRV) with the 10/11-mer DNA and 25-mer DNA-bound states. **b**, Stick representation of the 25-mer DNA duplex bound to the DNMT3A–DNMT3L tetramer, with the $2F_o - F_c$ omit map contoured at the 1σ level. **c**, The two helices of DNMT3A that interact with DNMT3L (shown in green) are coloured in pink (α4 and α5 in accordance with the numeration in Extended Data Fig. 3g) and preceded by two DNA contact loops, coloured in blue. The flipped out zebularine (Z5) is coloured in purple. The bound AdoHcy molecule is shown in sphere representation.

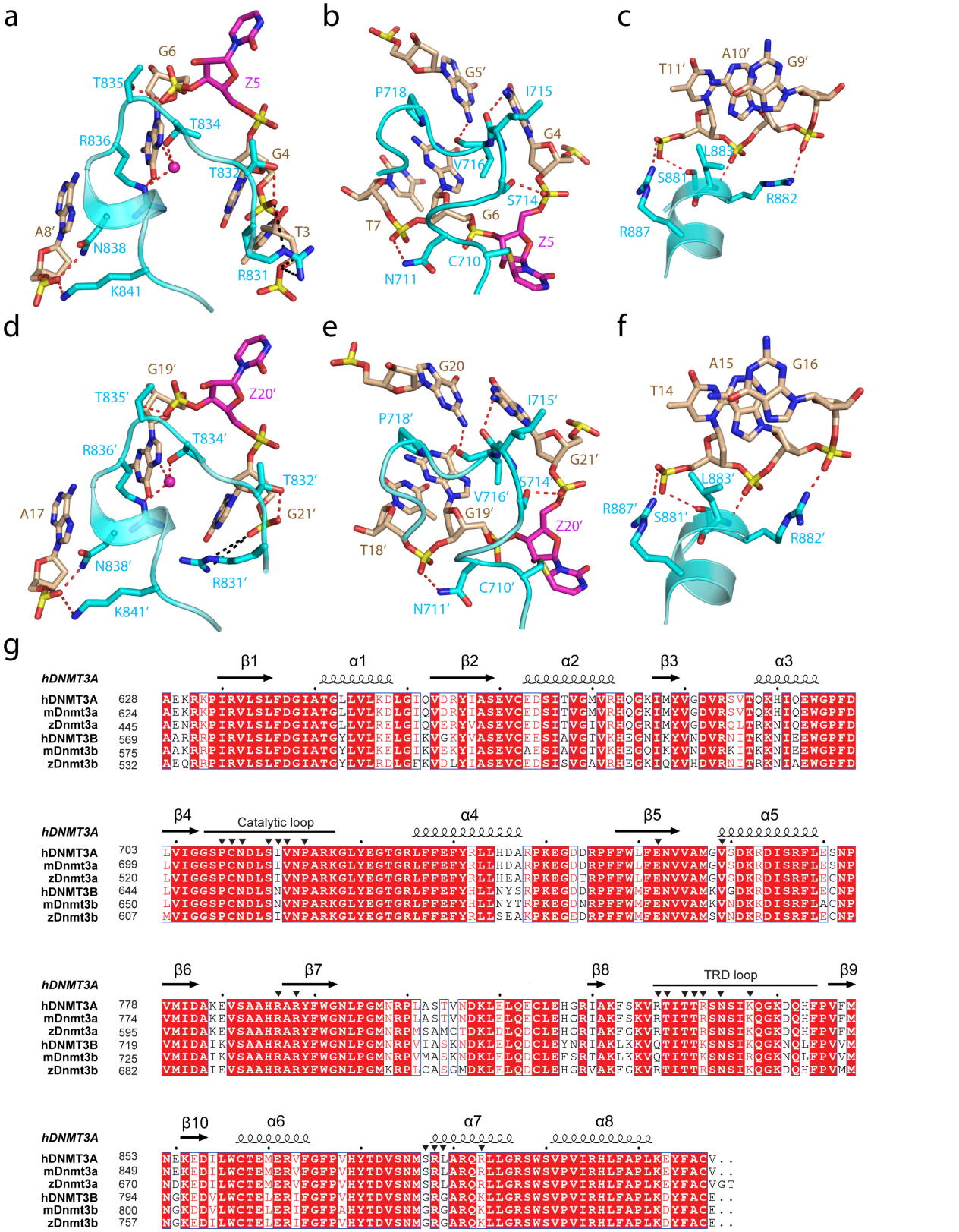

Extended Data Figure 3 | Various intermolecular interactions between the two DNMT3A monomers and DNA. a–f, DNA binding by the first and second DNMT3A monomer (defined as 3A and 3A′, respectively, in Fig. 1c) includes the intermolecular interactions between the TRD loop of DNMT3A and the DNA major groove (**a**, **d**), between the catalytic loop of DNMT3A and the DNA minor groove (**b**, **e**), and between the homodimeric interface of DNMT3A and the DNA backbone (**c**, **f**). The hydrogen-bonding interactions are shown as dashed lines. The water molecules are shown as purple spheres. **g**, Structure-based sequence alignment of DNMT3 proteins from human (hDNMT3A and hDNMT3B), mouse (mDnmt3a and mDnmt3b), and zebrafish (zDnmt3a and zDnmt3b). Completely conserved residues are coloured in white and highlighted in red. Partly conserved residues are coloured in red. Secondary structures are shown above the aligned sequences. The DNA-binding residues as revealed by this study are marked with black triangles.

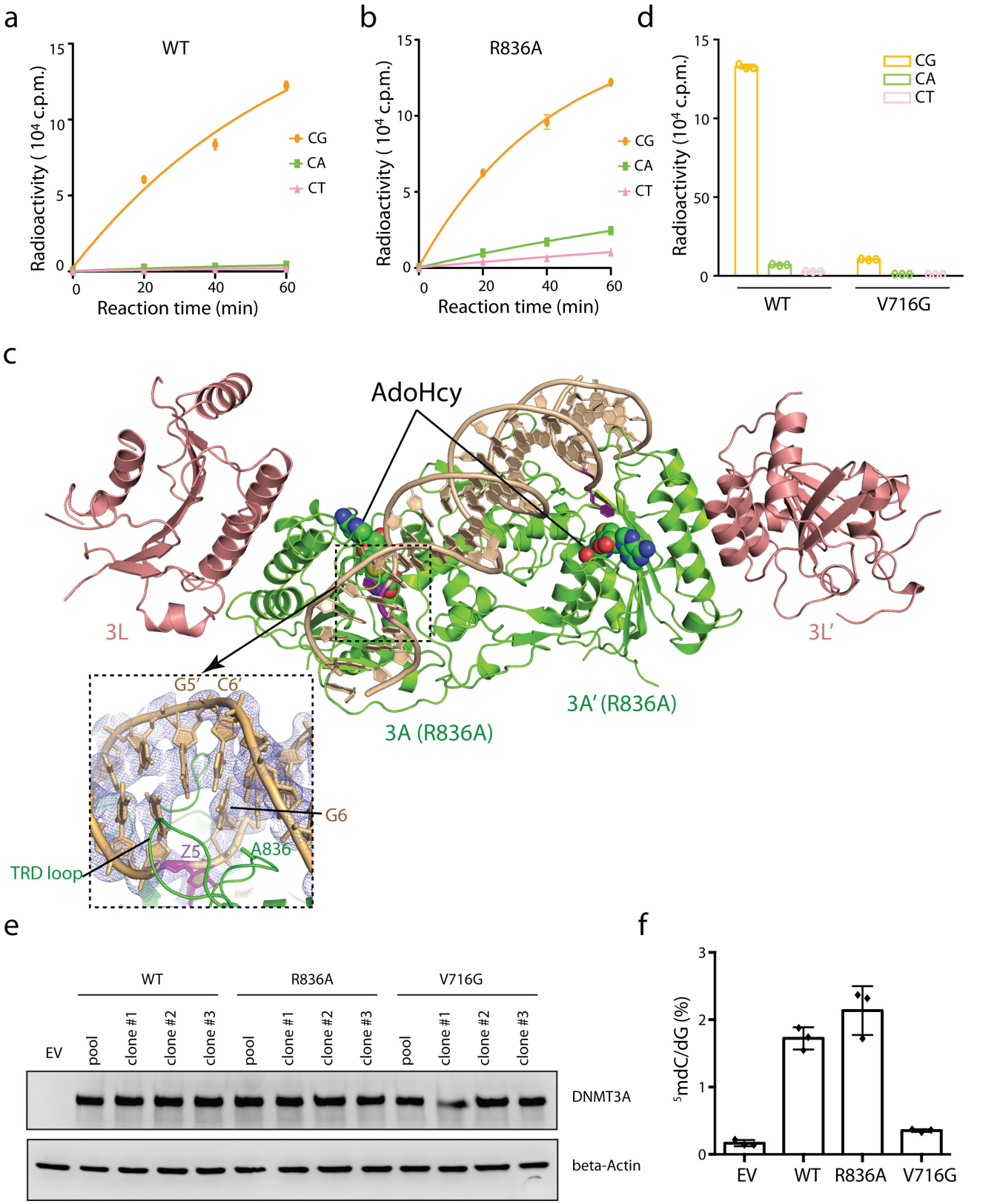

Extended Data Figure 4 | See next page for caption.

Extended Data Figure 4 | The essential roles for the CpG-engaging residues of DNMT3A, R836, and V716 in DNMT3A-mediated CpG versus non-CpG methylations. a, **b**, DNA methylation kinetics analysis of wild-type ($DNMT3A^{WT}$, **a**) and R836A-mutated ($DNMT3A^{R836A}$, **b**) DNMT3A using the CpG-, CpA-, or CpT-containing DNA substrates ($n = 3$ biological replicates). Purified DNMT3A–DNMT3L tetramer complex was used for measurements, followed by fitting with a first-order exponential equation. **c**, Ribbon representation of the crystal structure of $DNMT3A^{R836A}$–DNMT3L tetramer in complex with the 25-mer DNA, with the CpG recognition by one of the DNMT3A monomers shown in expanded view. The $2F_o - F_c$ omit map of DNA was contoured at the 0.8σ level, and coloured in light blue. **d**, Methylation assay using either $DNMT3A^{WT}$ or $DNMT3A^{V716G}$ on CG-, CA-, and CT-containing DNA ($n = 3$ biological replicates). **e**, Immunoblots detect reconstituted expression of the indicated DNMT3A among TKO mouse ES cells, either the pooled stable-expression cell population or single-cell-derived clonal lines. EV, empty vector. A representative blot of two independent experiments is shown. For gel Source Data, see Supplementary Fig. 1. **f**, LC–MS analysis reveals the global 5-methyl-2′-deoxycytidine (5-mdC) levels (calculated as 5-mdC/2′-deoxyguanosine on the *y* axis) in the TKO ES cells after stable transduction of empty vector or the indicated DNMT3A ($n = 3$ biological replicates). Data are mean ± s.d.

a

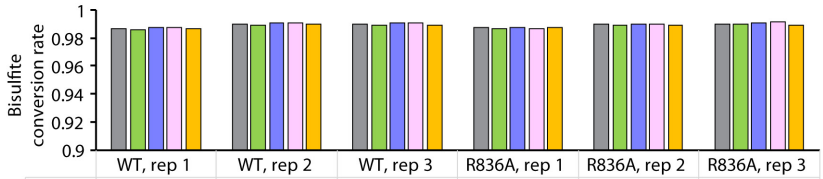

	WT, rep 1	WT, rep 2	WT, rep 3	R836A, rep 1	R836A, rep 2	R836A, rep 3
CpN	0.987	0.990	0.990	0.987	0.990	0.990
CpA	0.986	0.989	0.989	0.987	0.989	0.990
CpC	0.988	0.991	0.991	0.988	0.990	0.991
CpT	0.987	0.991	0.991	0.987	0.990	0.991
CpG	0.987	0.990	0.989	0.987	0.989	0.989

b

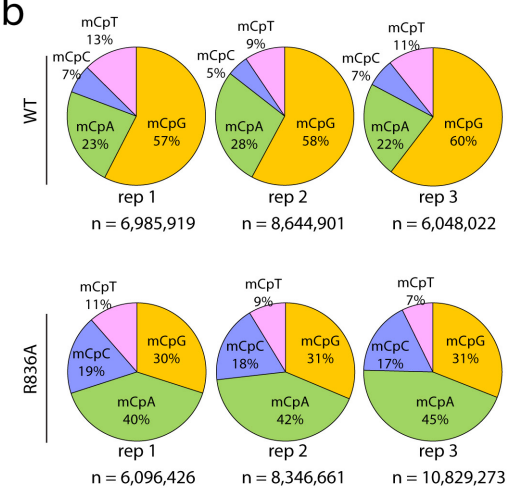

c

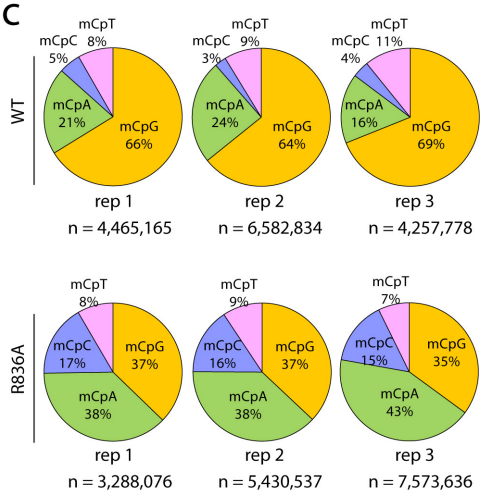

d

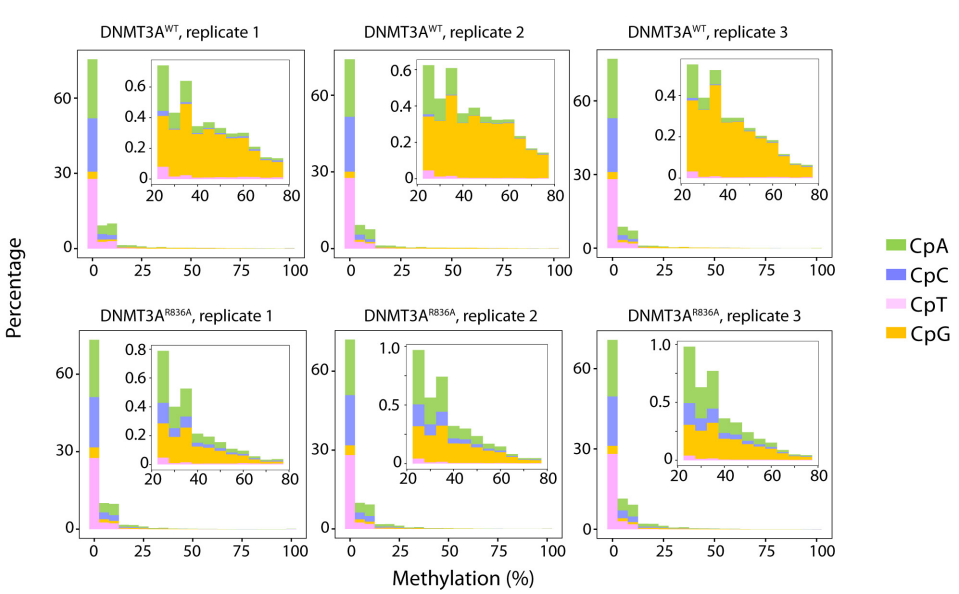

Extended Data Figure 5 | eRRBS reveals distribution of cytosine methylations in each sequence context among TKO ES cells with reconstituted expression of either DNMT3A^{WT} or DNMT3A^{R836A}. **a**, The rates of bisulfite conversion for the indicated sequence context in each sample as determined by the unmethylated lambda DNA spike-in control. CpN, all cytosines. **b**, **c**, Pie charts showing the percentage of methylated cytosines (total number *n* shown at the bottom of each plot) identified among the DNMT3A^{WT}- or DNMT3A^{R836A}-expressing TKO ES cells in each sequence context. The methylated cytosines were called using a stringent binomial distribution-based filter to eliminate false positives from incomplete bisulfite conversion, with an FDR of 1% and 0.1% set for **b** and **c**, respectively. **d**, Distribution of methylation levels (percentage on *x* axis) for the indicated sequence context. Inserts show a closed view of the distribution at sites with intermediate to high levels of cytosine methylation.

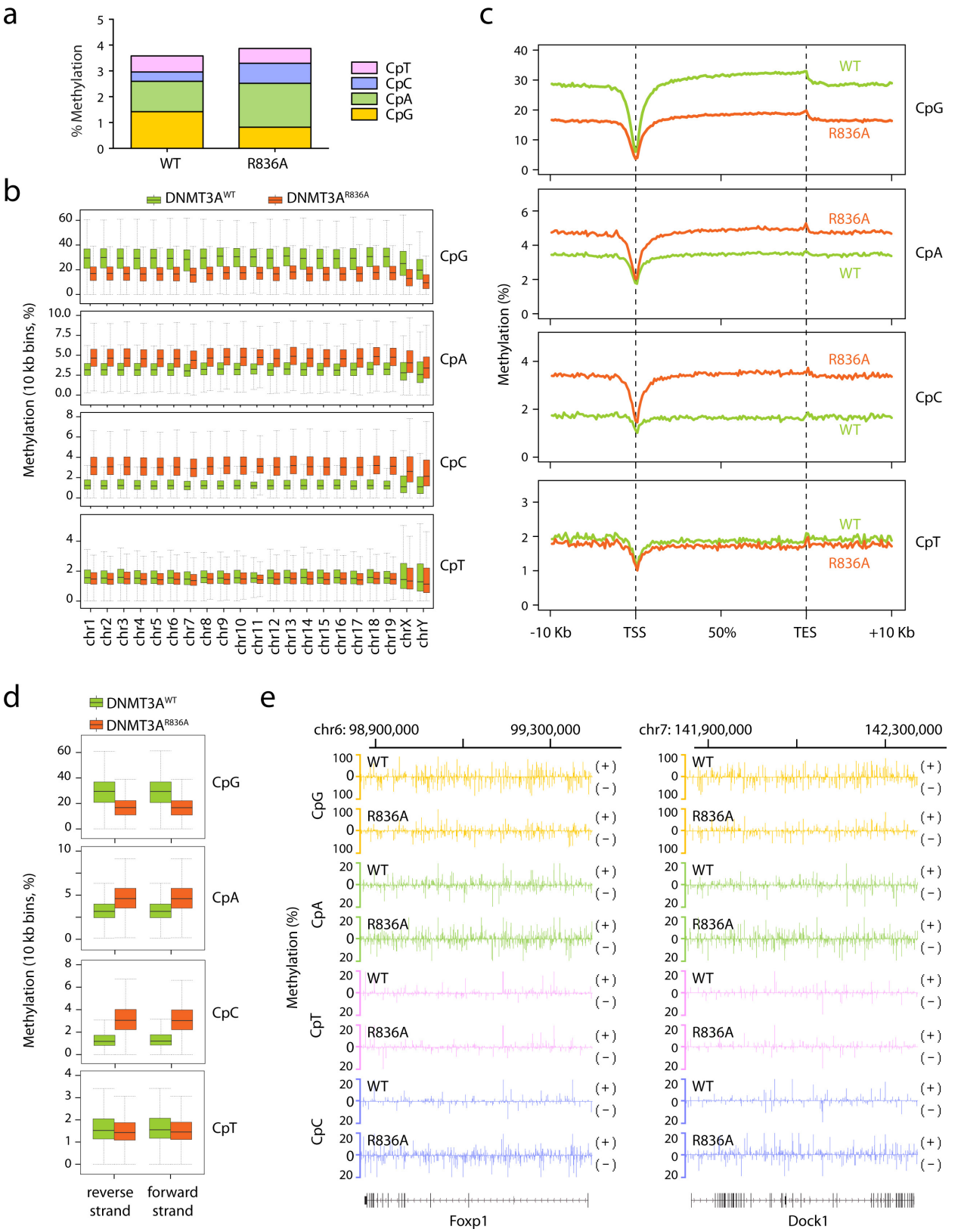

Extended Data Figure 6 | See next page for caption.

Extended Data Figure 6 | CpG and non-CpG methylations induced by DNMT3A^{WT} versus DNMT3A^{R836A} in the TKO ES cells. a, Overall methylation levels of cytosines at four different sequence contexts as detected by eRRBS. On the *y* axis, the averaged methylation level of all cytosines within the mouse genome is shown, as calculated by normalization of the detected methylation cytosines over total cytosine numbers in the TKO ES cells reconstituted with either DNMT3A^{WT} (left) or DNMT3A^{R836A} (right). **b**, Global levels of CpG and CpH (H = A, C, or T) methylation induced by DNMT3A^{WT} (green) or DNMT3A^{R836A} (red) across the mouse chromosomes of the TKO ES cells. Box and whisker plots of 10-kb-bin-averaged methylation levels of each mouse chromosome are shown. **c**, Global levels of CpG and CpH methylation induced by DNMT3A^{WT} (green) versus DNMT3A^{R836} (red) across all annotated genes. Each gene was divided into 100 equally sized bins and the 10-kb flanking region was divided into 50 equally sized bins. Averaged methylation levels were plotted for each bin. TSS, transcription start site; TES, transcription end site. **d**, Global levels of CpG and CpH methylation induced by DNMT3A^{WT} (green) versus DNMT3A^{R836A} (red) on the two opposite DNA strands. Boxplots of 10-kb-bin-averaged CpG, CpA, CpC, and CpT methylation levels of each strand are shown. **e**, Representative gene-wide views of CpG and CpH methylations at *Foxp1* and *Dock1*, which are grouped into either the forward (+) or reverse (−) DNA strand. Cytosines covered by at least 15 reads from eRRBS data are shown, with each site designated by a vertical line. Panels **a**–**e** use the combined dataset of three biological replicates per group. Box plots depict the interquartile range, and whiskers depict 1.5 × interquartile range.

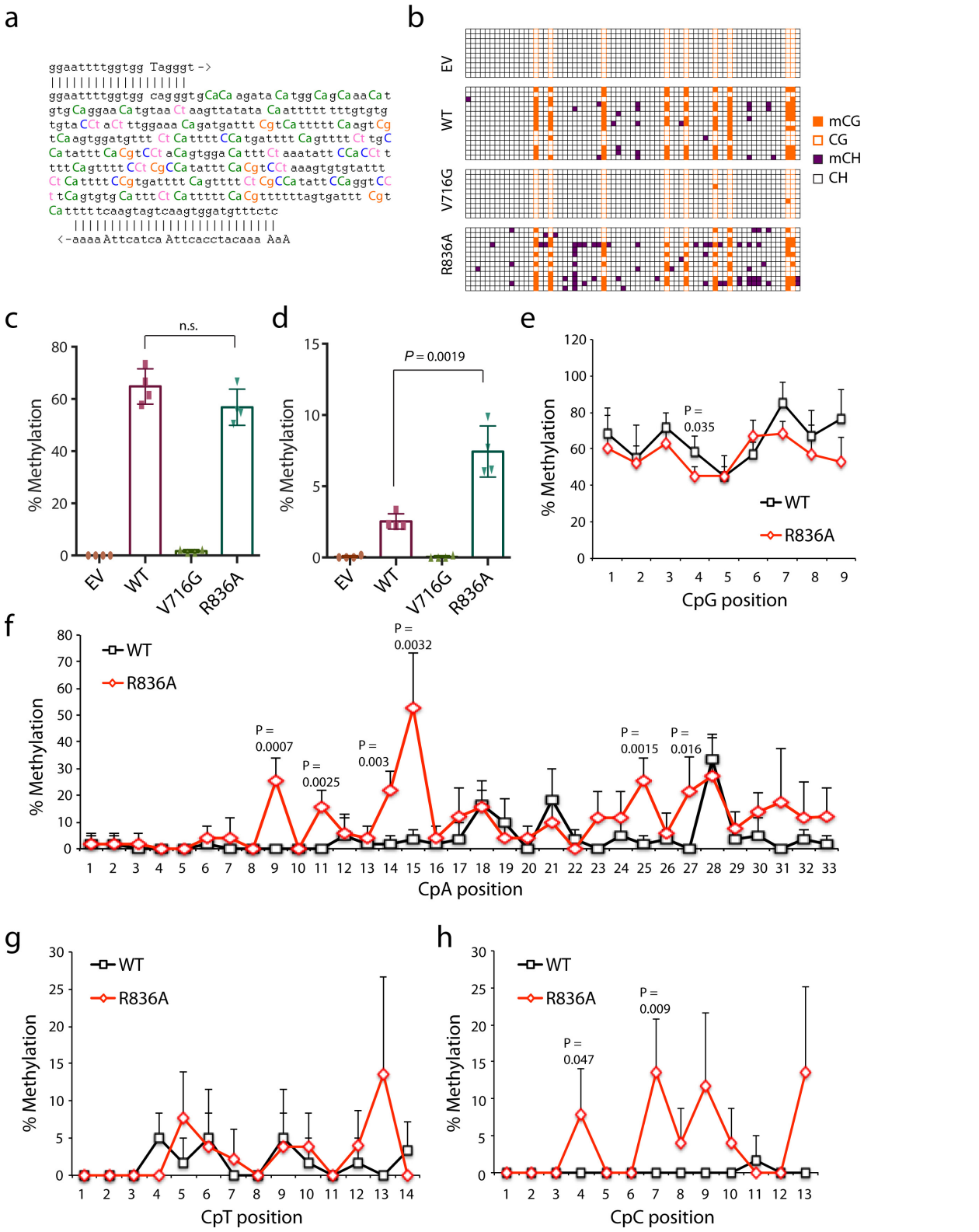

Extended Data Figure 7 | Sanger bisulfite sequencing to validate the cytosine methylation levels mediated by DNMT3A, either wild type or defective in recognizing the CpG substrate, among the TKO mouse ES cells. a, Sequence of the examined major satellite DNA region. Primers used for bisulfite PCR are denoted with 5′ and 3′ primer pairing. The counts for cytosines, highlighted in colour, are 9 for the CG dinucleotide, 33 for CA, 14 for CT, and 13 for CC. **b**, A representative result for bisulfite sequencing analysis of the major satellite repeat region described above in the TKO cells expressing empty vector, wild-type DNMT3A, or the indicated mutant. Each row represents one DNA clone and each column represents one site of cytosine, either methylated (filled) or unmethylated (open). **c**, **d**, Percentage of methylation mediated by DNMT3A or the indicated mutant at CpG (**c**) and non-CG (**d**) sites within the examined major satellite DNA region in the TKO ES cells. Data are mean ± s.d.; $n = 4$ independent bisulfite sequencing experiments as shown in **b**. **e**–**h**, Average cytosine methylation levels at each individual site grouped by the CpG (**e**), CpA (**f**), CpT (**g**), or CpC (**h**) context in the examined major satellite DNA among the TKO ES cells reconstituted with $DNMT3A^{WT}$ versus $DNMT3A^{R836A}$ ($n = 4$ biological replicates; mean ± s.d., with the labelled *P* values). Statistical analysis used a two-tailed Student's *t*-test; NS, not significant.

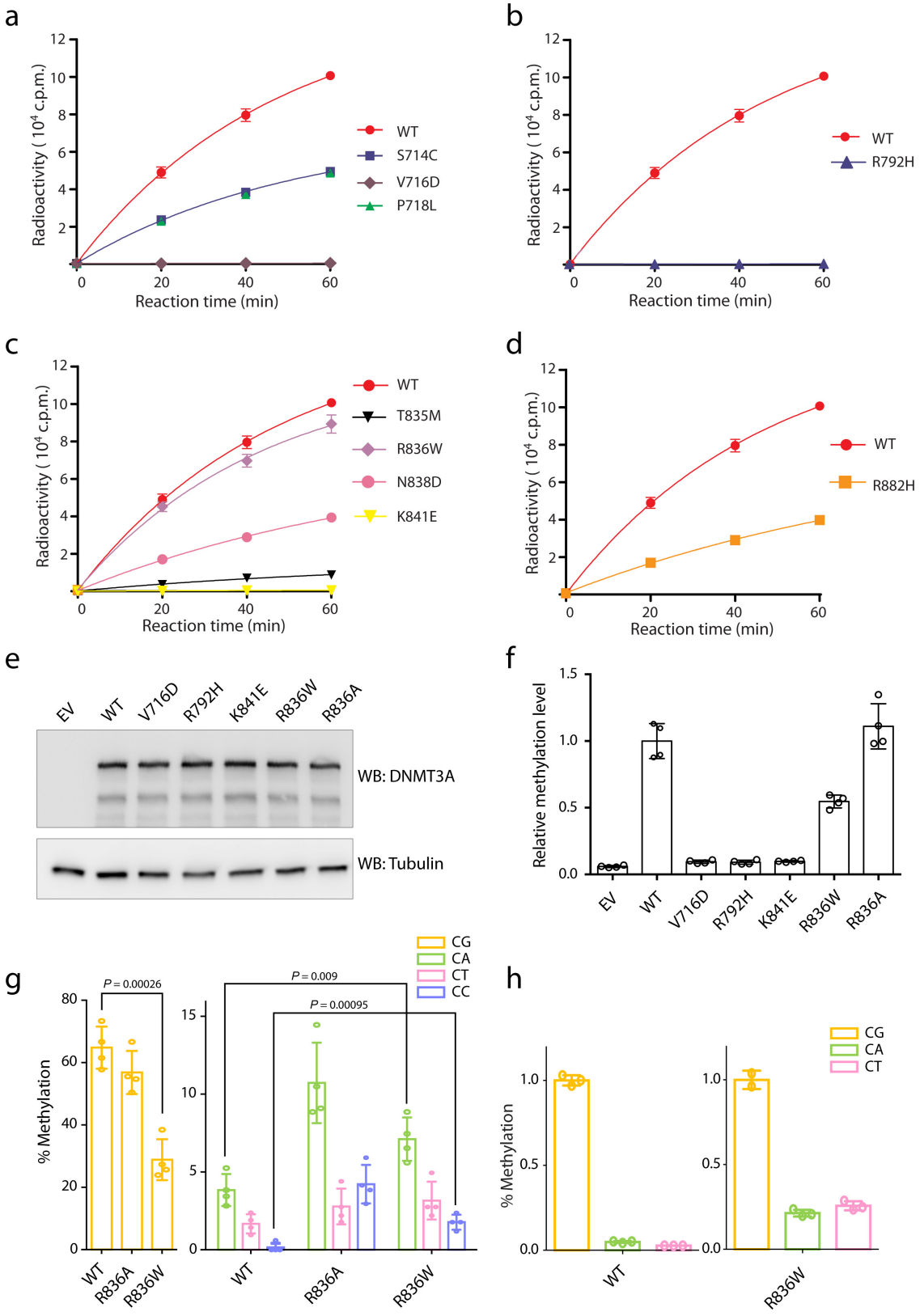

Extended Data Figure 8 | See next page for caption.

Extended Data Figure 8 | Effect of haematological cancer-associated mutations of DNMT3A on DNA methylation *in vitro* and in mouse TKO ES cells. a, Methylation kinetics of DNMT3A with mutations located at the catalytic loop, compared with $DNMT3A^{WT}$. **b**, Methylation kinetics of DNMT3A with an active site mutation, R792H. **c**, Methylation kinetics of DNMT3A with mutations located at the TRD loop. **d**, Methylation kinetics of DNMT3A with the hotspot mutation R882H. For **a**–**d**, DNMT3A–DNMT3L complex was used for the measurements ($n = 3$ biological replicates), followed by fitting with a first-order exponential equation. These data were measured independently from those shown in Fig. 4c. **e**, Immunoblot detects stable reconstitution of $DNMT3A^{WT}$ or the indicated DNMT3A mutant in the TKO ES cells. A representative blot of two independent experiments is shown. For gel Source Data, see Supplementary Fig. 1. **f**, LC–MS analysis reveals the global 5-methyl-2′- deoxycytidine (5-mdC) levels (calculated as 5-mdC/2′-deoxyguanosine) in the TKO ES cells after stable transduction of empty vector or the indicated DNMT3A. The methylation levels relative to TKO cells expressing $DNMT3A^{WT}$ are plotted. Data are mean ± s.d.; $n = 4$ biological replicates. **g**, Individual bisulfate sequencing detects the methylation level of cytosines in each sequence context within a major satellite DNA site at chromosome 2 in the TKO cells reconstituted with $DNMT3A^{R836W}$ (right), compared with $DNMT3A^{WT}$ (left) or $DNMT3A^{R836A}$ (middle; as determined in Fig. 3g) (n = 4; mean ± s.d.). Statistical analysis used a two-tailed Student's *t*-test. **h**, *In vitro* methylation of CG-, CA-, or CT-containing DNA using $DNMT3A^{WT}$ (left) or $DNMT3A^{R836W}$ (right) in complex with DNMT3L, reacted for 40 min ($n = 3$ biological replicates). The methylation levels relative to CG-containing DNA substrates are plotted. Data are mean ± s.d.

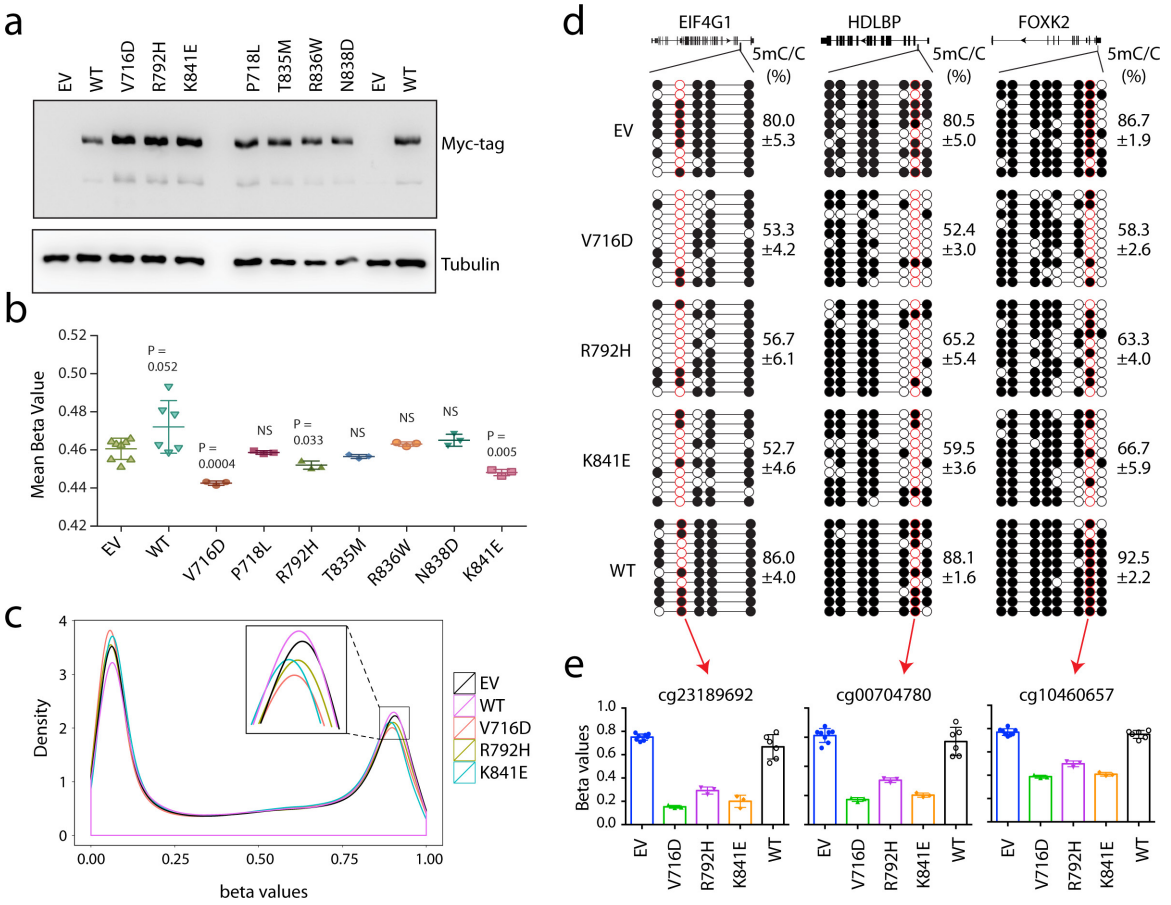

Extended Data Figure 9 | Effect of haematological cancer-associated mutations of DNMT3A on genomic DNA methylation in the TF-1 leukaemia cells. a, Immunoblot of the TF-1 cells stably transduced with Myc-tagged DNMT3A, either wild type or the indicated cancer-associated mutants. EV, empty MSCV vector. A representative blot of two independent experiments is shown. For gel Source Data, see Supplementary Fig. 1. **b**, Profiling of the indicated DNMT3A-expressing TF-1 cell lines with the HumanMethylation_450K BeadChip array reveals the mean methylation β values for all examined CpGs. Each dot represents a biological replicate: that is, an independently derived stable-expression cell line ($n = 3$–8 biological replicates per group; mean ± s.d.). Statistical analysis used a two-tailed Student's *t*-test. **c**, Density plot of methylation β values for all examined CpGs in the indicated DNMT3A-expressing TF-1 cell lines. The inserted box shows a zoom-in view for densities for highly methylated DNA sites among the indicated samples. Data are mean ± s.d., with the labelled *P* values. Statistical analysis used two-tailed Student's *t*-test. **d**, Sanger bisulfite sequencing of the indicated regions from TF-1 cell lines stably transduced with empty vector, $DNMT3A^{WT}$ or the indicated cancer-associated mutant. Individual CpG sites (circles) are filled with black (methylated) or white (unmethylated). Red circles denote the CpG sites covered by the Illumina Infinium 450K DNA methylation array. Data are mean ± s.d.; $n = 3$ biological replicates. **e**, Methylation values of the indicated CpG sites (labelled by red circles in **d**) based on the measurements with the Infinium 450K DNA methylation arrays ($n = 3$–8 biological replicates; mean ± s.d.).

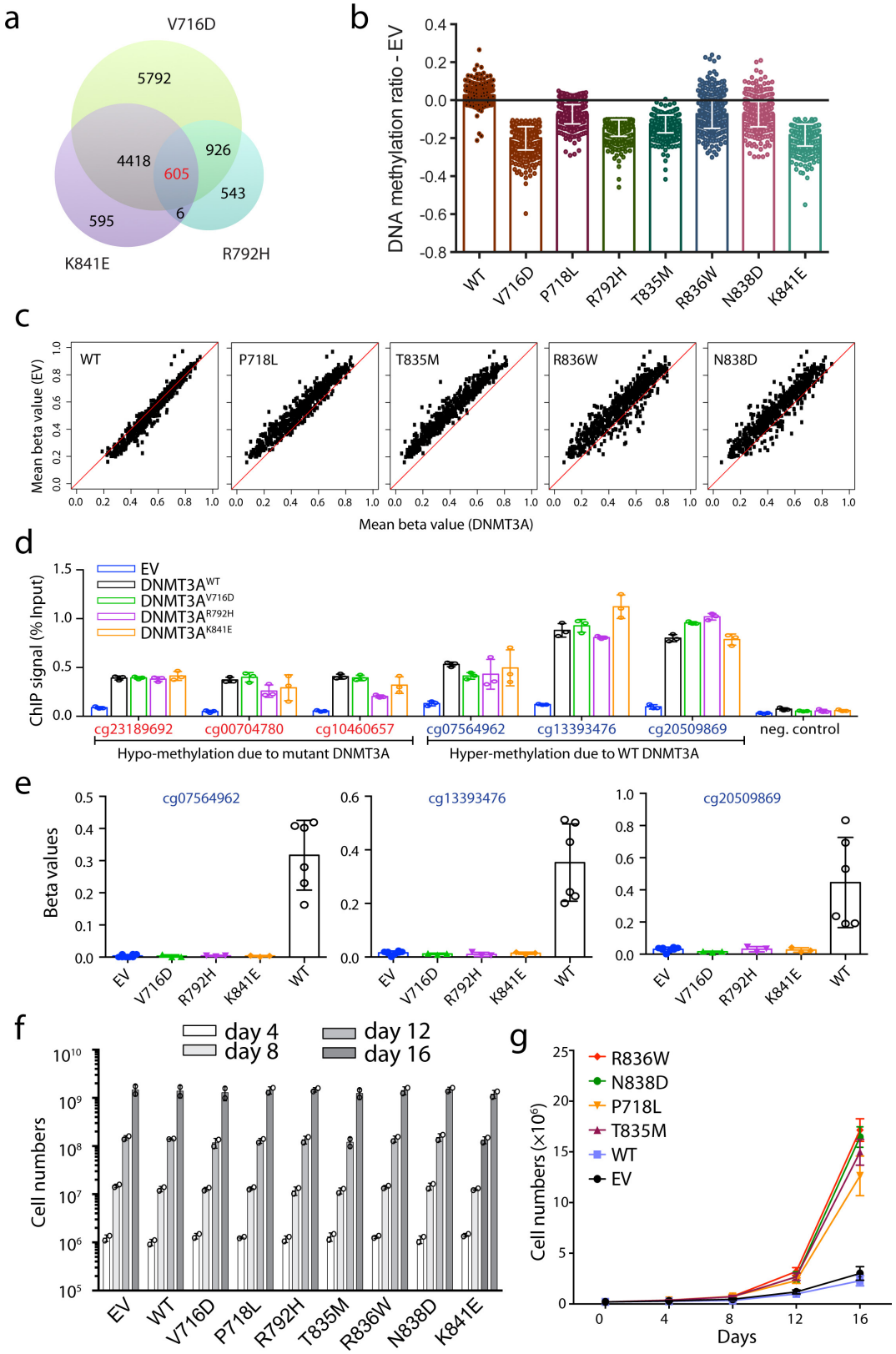

Extended Data Figure 10 | See next page for caption.

Extended Data Figure 10 | Effect of haematological cancer-associated DNMT3A mutations on DNA hypomethylation and cytokine-independent growth of the TF-1 leukaemia cells. a, Venn diagram of CpG sites with hypomethylation induced by either one of the three indicated strong DNA-binding-defective mutants of DNMT3A, V716D, K841E, and R792H. **b**, **c**, Bar plots (**b**) and scatter plots (**c**) showing methylation difference at the 605 commonly hypomethylated CpG sites identified in **a** among the TF-1 cells with stable transduction of either $DNMT3A^{WT}$ or the indicated mutant, compared with empty MSCV vector. A black line in **b** indicates empty vector control ($n = 3$–8 biological replicates per group; mean ± s.d.). In **c**, mean methylation β values are plotted of each individual CpG in the indicated DNMT3A experimental group (x axis) and control empty vector group (y axis; $n = 3$–8 biological replicates per group). **d**, **e**, Comparable occupancy of DNMT3A and its mutant forms at the indicated genomic loci with affected DNA methylation, as measured by ChIP analysis of the Myc-tagged $DNMT3A^{WT}$ or mutants in TF-1 stable-expression cell lines. Tested sites by ChIP–qPCR in **d** ($n = 3$ biological replicates; mean ± s.d.) included three CpG sites showing hypomethylation due to expression of mutant DNMT3A (left; also see Extended Data Fig. 9e), three sites showing hypermethylation due to expression of $DNMT3A^{WT}$ (middle; also see **e**, which shows mean methylation β values from measurements with the Infinium 450K DNA methylation arrays, $n = 3$–8 biological replicates; mean ± s.d.), and a negative control locus (right; the GAPDH transcription start site). The anti-Myc antibody was used for ChIP and the empty-vector-expressing TF-1 cells used as cell control for unspecific binding. **f**, Proliferation of the indicated DNMT3A stable-expression TF-1 cells in the presence of a supporting cytokine, GM-CSF ($n = 2$ biological replicates; mean ± s.d.). **g**, Proliferation of the indicated DNMT3A-expressing TF-1 cells after GM-CSF withdrawal ($n = 3$ biological replicates; mean ± s.d.).

nature research

Corresponding author(s): Gang Greg Wang; Jikui Song

Life Sciences Reporting Summary

Nature Research wishes to improve the reproducibility of the work that we publish. This form is intended for publication with all accepted life science papers and provides structure for consistency and transparency in reporting. Every life science submission will use this form; some list items might not apply to an individual manuscript, but all fields must be completed for clarity.

For further information on the points included in this form, see Reporting Life Sciences Research. For further information on Nature Research policies, including our data availability policy, see Authors & Referees and the Editorial Policy Checklist.

Please do not complete any field with "not applicable" or n/a. Refer to the help text for what text to use if an item is not relevant to your study.

For final submission: please carefully check your responses for accuracy; you will not be able to make changes later.

Experimental design

1. Sample size

   Describe how sample size was determined.

   For various in vitro DNA methylation assays (Fig. 3c, 4c, Extended Data Fig. 4a,b,d, and Extended Data Fig. 8a-d,h), three biological replicates were used and stated in figure legends. For cellular and genomics assays (Fig. 3d-g, Fig. 4d-f, Extended Data Fig. 4e,f, Extended Data Fig. 5-7, Extended Data Fig. 8e-g, and Extended Data Fig. 9-10), at least three biological replicates were used and stated in figure legends.

2. Data exclusions

   Describe any data exclusions.

   One data point from Extended Data Fig.4a, three data points from Extended Data Fig. 8a-d and one data point from Extended Data Fig. 8h were identified as outliers and were excluded from analysis.

3. Replication

   Describe the measures taken to verify the reproducibility of the experimental findings.

   Data are presented as the mean ± SD of at least three independent experiments. Statistical analysis was performed with Student's t test for comparing two sets of data with assumed normal distribution. A p value of less than 0.05 was considered to be significant.

4. Randomization

   Describe how samples/organisms/participants were allocated into experimental groups.

   N/A

5. Blinding

   Describe whether the investigators were blinded to group allocation during data collection and/or analysis.

   N/A

Note: all in vivo studies must report how sample size was determined and whether blinding and randomization were used.

6. Statistical parameters

For all figures and tables that use statistical methods, confirm that the following items are present in relevant figure legends (or in the Methods section if additional space is needed).

n/a	Confirmed
☐	☒ The exact sample size (*n*) for each experimental group/condition, given as a discrete number and unit of measurement (animals, litters, cultures, etc.)
☐	☒ A description of how samples were collected, noting whether measurements were taken from distinct samples or whether the same sample was measured repeatedly
☐	☒ A statement indicating how many times each experiment was replicated
☐	☒ The statistical test(s) used and whether they are one- or two-sided *Only common tests should be described solely by name; describe more complex techniques in the Methods section.*
☐	☒ A description of any assumptions or corrections, such as an adjustment for multiple comparisons
☐	☒ Test values indicating whether an effect is present *Provide confidence intervals or give results of significance tests (e.g. P values) as exact values whenever appropriate and with effect sizes noted.*
☐	☒ A clear description of statistics including central tendency (e.g. median, mean) and variation (e.g. standard deviation, interquartile range)
☐	☒ Clearly defined error bars in all relevant figure captions (with explicit mention of central tendency and variation)

See the web collection on statistics for biologists for further resources and guidance.

Software

Policy information about availability of computer code

7. Software

Describe the software used to analyze the data in this study.

For structural study, the HKL2000, XDS, PHENIX, Coot and Pymol softwares were used for data processing and analysis. For eRRBS analysis, 'Bismark' software package was used. For DNA methylation array analysis, the R 'minfi' software package was used. Custom scripts used for eRRBS and 450K array analyses are available upon request.

For manuscripts utilizing custom algorithms or software that are central to the paper but not yet described in the published literature, software must be made available to editors and reviewers upon request. We strongly encourage code deposition in a community repository (e.g. GitHub). *Nature Methods* guidance for providing algorithms and software for publication provides further information on this topic.

Materials and reagents

Policy information about availability of materials

8. Materials availability

Indicate whether there are restrictions on availability of unique materials or if these materials are only available for distribution by a third party.

No restrictions

9. Antibodies

Describe the antibodies used and how they were validated for use in the system under study (i.e. assay and species).

Antibodies used for western blotting were α-MYC (Sigma, 9E10), α-DNMT3A (Santa Cruz, H-295), anti-beta-Actin (Santa Cruz, sc-47778) and α-tubulin (Sigma). They were validated by the manufacturers.

10. Eukaryotic cell lines

a. State the source of each eukaryotic cell line used.

Dnmt3a, Dnmt3b and Dnmt1 triple knockout (TKO) mouse ES cells was a kind gift from Dr. Masaki Okano, RIKEN Center for Developmental Biology. The TF-1 human erythroleukemic cell line was obtained from ATCC.

b. Describe the method of cell line authentication used.

Authentication of cell line identity, including that of parental and derived lines, was ensured by Tissue Culture Facility affiliated to the Lineberger Comprehensive Cancer Center of UNC at Chapel Hill using the genetic signature profiling and fingerprinting analysis.

c. Report whether the cell lines were tested for mycoplasma contamination.

Every 1-2 month, a routine examination of cell lines in culture for any possible mycoplasma contamination was carried out using MycoAlert Mycoplasma Detection Kit (Lonza).

d. If any of the cell lines used are listed in the database of commonly misidentified cell lines maintained by ICLAC, provide a scientific rationale for their use.

N/A

Animals and human research participants

Policy information about studies involving animals; when reporting animal research, follow the ARRIVE guidelines

11. Description of research animals

Provide all relevant details on animals and/or animal-derived materials used in the study.

N/A

Policy information about studies involving human research participants

12. Description of human research participants

Describe the covariate-relevant population characteristics of the human research participants.

N/A